Metamorphic and Metasomatic Kyanite-Bearing Mineral Assemblages of Thassos Island (Rhodope, Greece)

Alexandre Tarantola, Panagiotis Voudouris, Aurélien Eglinger, Christophe Scheffer, Kimberly Trebus, Marie Bitte, Benjamin Rondeau, Constantinos Mavrogonatos, Ian Graham, Marius Etienne, et al.

minerals

MDPI

Article

Metamorphic and Metasomatic Kyanite-Bearing Mineral Assemblages of Thassos Island (Rhodope, Greece)

Alexandre Tarantola [1,*], Panagiotis Voudouris [2], Aurélien Eglinger [1], Christophe Scheffer [1,3], Kimberly Trebus [1], Marie Bitte [1], Benjamin Rondeau [4], Constantinos Mavrogonatos [2], Ian Graham [5], Marius Etienne [1] and Chantal Peiffert [1]

1 GeoRessources, Faculté des Sciences et Technologies, Université de Lorraine, CNRS, F-54506 Vandœuvre-lès-Nancy, France; aurelien.eglinger@univ-lorraine.fr (A.E.); christophe.scheffer.1@ulaval.ca (C.S.); kimberly.trebus5@etu.univ-lorraine.fr (K.T.); marie.bitte8@etu.univ-lorraine.fr (M.B.); marius.etienne5@gmail.com (M.E.); chantal.peiffert@univ-lorraine.fr (C.P.)

2 Department of Geology & Geoenvironment, National and Kapodistrian University of Athens, 15784 Athens, Greece; voudouris@geol.uoa.gr (P.V.); kmavrogon@geol.uoa.gr (C.M.)

3 Département de Géologie et de Génie Géologique, Université Laval, Québec, QC G1V 0A6, Canada

4 Laboratoire de Planétologie et Géodynamique, Université de Nantes, CNRS UMR 6112, 44322 Nantes, France; benjamin.rondeau@univ-nantes.fr

5 PANGEA Research Centre, School of Biological, Earth and Environmental Sciences, University of New South Wales, Sydney, NSW 2052 Australia; i.graham@unsw.edu.au

* Correspondence: alexandre.tarantola@univ-lorraine.fr; Tel.: +33-3-72-74-55-67

Received: 27 February 2019; Accepted: 23 April 2019; Published: 25 April 2019

Abstract: The Trikorfo area (Thassos Island, Rhodope massif, Northern Greece) represents a unique mineralogical locality with Mn-rich minerals including kyanite, andalusite, garnet and epidote. Their vivid colors and large crystal size make them good indicators of gem-quality materials, although crystals found up to now are too fractured to be considered as marketable gems. The dominant lithology is represented by a garnet–kyanite–biotite–hematite–plagioclase ± staurolite ± sillimanite paragneiss. Thermodynamic Perple_X modeling indicates conditions of ca. 630–710 °C and 7.8–10.4 kbars. Post-metamorphic metasomatic silicate and calc-silicate (Mn-rich)-minerals are found within (i) green-red horizons with a mineralogical zonation from diopside, hornblende, epidote and grossular, (ii) mica schists containing spessartine, kyanite, andalusite and piemontite, and (iii) weakly deformed quartz-feldspar coarse-grained veins with kyanite at the interface with the metamorphic gneiss. The transition towards brittle conditions is shown by Alpine-type tension gashes, including spessartine–epidote–clinochlore–hornblende-quartz veins, cross-cutting the metamorphic foliation. Kyanite is of particular interest because it is present in the metamorphic paragenesis and locally in metasomatic assemblages with a large variety of colors (zoned blue to green/yellow-transparent and orange). Element analyses and UV-near infrared spectroscopy analyses indicate that the variation in color is due to a combination of Ti^{4+}–Fe^{2+}, Fe^{3+} and Mn^{3+} substitutions with Al^{3+}. Structural and mineralogical observations point to a two-stage evolution of the Trikorfo area, where post-metamorphic hydrothermal fluid circulation lead locally to metasomatic reactions from ductile to brittle conditions during Miocene exhumation of the high-grade host-rocks. The large variety of mineral compositions and assemblages points to a local control of the mineralogy and fO_2 conditions during metasomatic reactions and interactions between hydrothermal active fluids and surrounding rocks.

Keywords: kyanite; Mn-rich silicates; Rhodope; Thassos; amphibolite facies; metasomatism

1. Introduction

Dispersed metal ions in substitution for Al and Si may lead to a large variety of colors in calc- and alumino-silicate minerals, e.g., [1,2]. For instance, the most common natural color of kyanite is blue but it can also be green, yellow, orange, white, black, grey or colorless as a function of the nature of elemental substitutions [3,4]. Kyanite is composed of usually >98 wt. % Al_2O_3 and SiO_2. The ~2 wt. % left is generally dominated by Fe, Ti, Mg, Mn, Cr and V. The variation in blue colors is attributed to Ti and/or Fe substitution and intervalence charge transfers within the crystal lattice [5], while the orange color of kyanite is generally attributed to the presence of Mn^{3+} [1,6–9]. The incorporation of trace elements is interpreted as the result of (i) oxygen fugacity during crystal growth (Fe), (ii) metamorphic grade, temperature of formation (Ti), or the nature of the protolith (Cr and V) [4]. In the same way, Mn^{3+} may substitute for Al^{3+} in andalusite [10,11] resulting in the dark green Mn-rich variety of andalusite, formerly known as viridine [2,12]. This may also be the case for epidotes e.g., [13], garnets e.g., [14] and other metamorphic and metasomatic Ca-Al silicates. Among the interesting trace elements to produce gem quality calc- and alumino-silicate minerals, Mn seems to play an important role. High-*PT* manganian silicate and calc-silicate metamorphic assemblages are very rare on Earth and require very specific conditions such as the preservation of high fO_2 during the entire metamorphic cycle, e.g., [15,16]. The presence in the protolith of Mn-oxides capable of buffering fO_2 to high levels during metamorphism as well as low fluid/rock ratio during the whole geodynamic evolution are necessary [17,18]. The best way to produce gem-quality Mn-rich silicates seems thus hydrothermal fluid circulation through an already Mn-rich protolith.

The geology of Greece is marked by a recent alpine belt, which results in outstanding localities for minerals and gemstones owing to high *PT* metamorphic conditions and subsequent magmatism and hydrothermalism, e.g., [19–23]. Among these localities, the island of Thassos, in the Rhodope Belt, represents a unique mineralogical locality for kyanite and uncommon varieties of manganiferous/manganian and magnesian silicate and calc-silicate minerals, including garnet, andalusite and epidote among others [19,24–31]. These crystals are often large (several centimeters long) and vividly colored, translucent but commonly fractured, which makes them usually inappropriate for faceting gemstones, but more proper for cabochon-shaped material. However, considering the extent of the geological units, their occurrence is promising for gemstones exploration in the area. In this article, we use the term "near gem-quality" as a reference to their aesthetic aspect (large size and vivid color) rather than to their potential as facetable material.

Thassos Island is part of the Southern Rhodope Metamorphic Core Complex (SRCC), with *PT* conditions recorded by the garnet–kyanite–biotite–hematite–plagioclase ± staurolite ± sillimanite assemblage of the paragneisses of the Trikorfo area (intermediate unit) in the range 600–650 °C, 4–7 kbars [24]. At the Trikorfo area, four main distinct lithologies, often bearing Ca-, Mg- and Mn-rich silicates, are distinguished with (i) the dominant metamorphic lithology composed of metasedimentary rocks, mostly mica schists and paragneisses, with intercalation of carbonate layers especially towards the base and top of the formation [24], (ii) green to red horizons parallel to the regional foliation enriched in silicate and calc-silicate minerals always showing a typical mineralogical zonation from the contact with the paragneisses/mica schists to the center of the layers, (iii) kyanite-andalusite bearing mica schists, and (iv) kyanite–quartz ± feldspar ± andalusite weakly deformed coarse-grained veins. The transition to brittle deformation conditions is shown by quartz–clinochlore–ilmenite–adularia–albite alpine-type tension gashes cross-cutting the metamorphic foliation [25]. Locally, when cross-cutting Mn-rich layers, these brittle veins can host spessartine and Mn-bearing clinochlore, epidote and hornblende.

On the basis of the description made by Voudouris et al. [20], the aim of the present study is (i) to obtain a complete inventory of the metamorphic and metasomatic minerals and their assemblages found at the Trikorfo site, (ii) to evaluate the cation substitution responsible for the color variations, (iii) to reevaluate the *PT* conditions attained by the gneiss host-rock on the basis of a comprehensive petrological phase equilibria using the Perple_X program, and (iv) to discuss the conditions of formation, metamorphic versus metasomatic, of these exceptional parageneses and assemblages of

(Mn-rich)-silicate and calc-silicate minerals. Kyanite, as a ubiquitous silicate found in both metamorphic and localized metasomatic assemblages, is the referent mineral described in the manuscript.

2. Geological Context

2.1. The Southern Rhodope Core Complex and Thassos Island

The Aegean domain, which extends from the Rhodope Massif in the north to the island of Crete in the south of the Hellenides, is a broad metamorphic domain whose formation started with the subduction of the Adriatic microplate (the northern part of the Africa Plate) below the Eurasia Plate, in late Cretaceous to Eocene times, e.g., [32–35]. The progressive southward retreat of the downgoing slab since the Oligocene is responsible for the exhumation of metamorphic core complexes (MCC) along low-angle detachment faults [36]. The Southern Rhodope Core Complex (SRCC) [37–41] and the Attic-Cycladic Metamorphic Complex (ACMC) [42–44] are the two main metamorphic domains resulting from Aegean extension during the Oligocene to Miocene. The Aegean domain is now in a back-arc position and the subduction front is currently located to the south of the island of Crete [35]. The SRCC, located in the northern part of Greece, displays an almost triangular shape and extends to south to southern Bulgaria [40]. It is mainly constituted by the Vertiskos Gneiss Complex from the Serbo-Macedonian Massif and to the west by the Chalkidiki Peninsula dominated by gneisses from the Sideroneron Massif (Figure 1). The area is marked by Jurassic and Cretaceous age ultra-high-pressure metamorphic events, including kyanite eclogites, followed by Barrovian type metamorphism, e.g., [37–41].

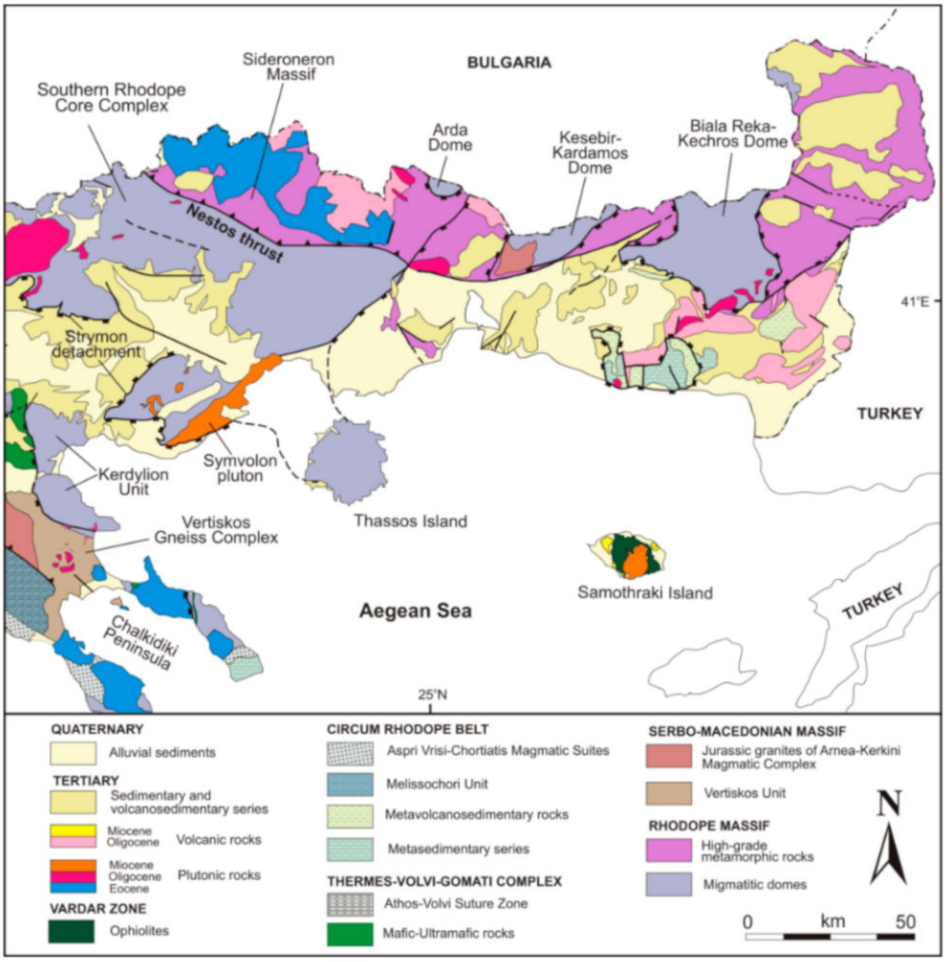

Figure 1. Geological map and regional tectonic framework of northern Greece, modified after Melfos and Voudouris [45].

Thassos Island, with an area of 400 km^2, exposes the south-east end of the SRCC. The geology of the island is dominated by the juxtaposition of shallow-dipping units mainly made of marbles, orthogneisses and paragneisses/mica schists (Figure 2). It is assumed that orthogneisses are the result of metamorphism of Hercynian plutonic units of the Greek Rhodope Massif [36,46] and that the protoliths of marbles and mica schists correspond to the Mesozoic sedimentary cover overlying the Hercynian plutonic basement.

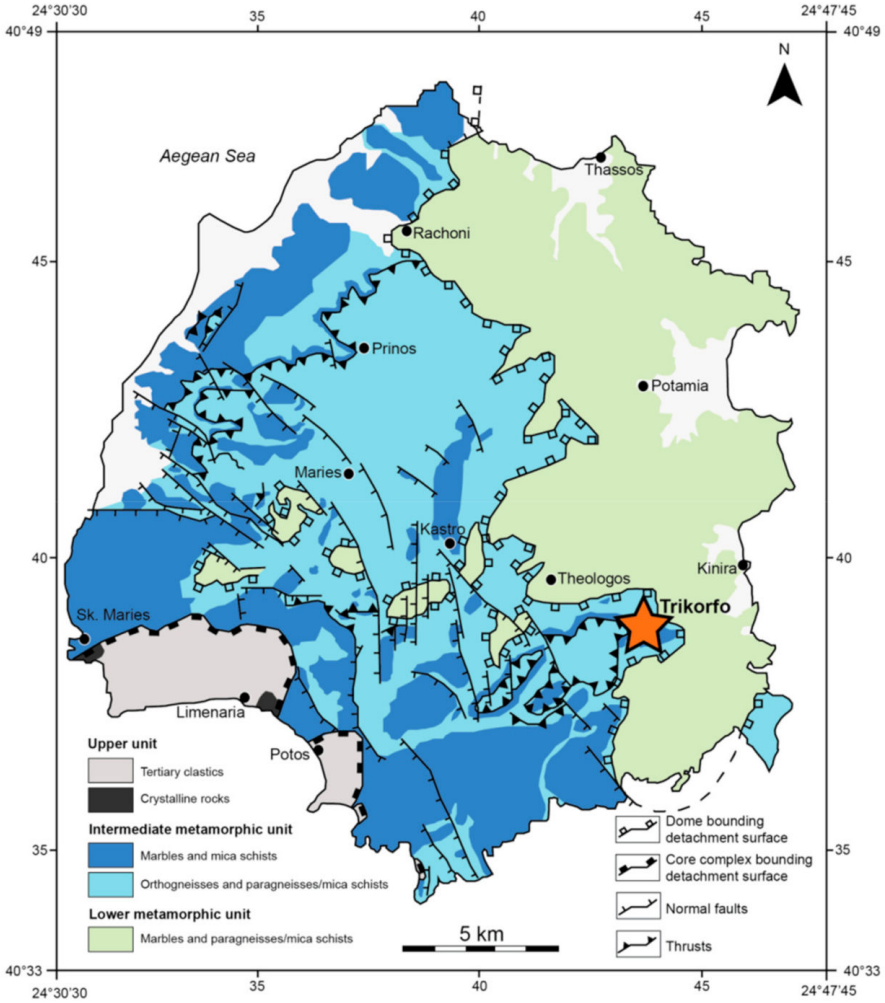

Figure 2. Geological map of Thassos Island with main units, modified from Wawrzenitz and Krohe [36] and Brun and Sokoutis [40]. The location of the Trikorfo area is indicated with an orange star.

Thassos Island is represented by three main metamorphic units with, from base to top, (i) the lower metamorphic unit dominated by mylonitic marbles with intercalations of mica schists and paragneisses forming metamorphic domes to the east of the island, (ii) an intermediate metamorphic unit composed at the base of gneisses overlapped by marbles with paragneiss, mica schist and amphibolite intercalations, (iii) the upper unit is considered as the hanging wall, consisting of non-mylonitic metamorphic rocks dominated by gneisses, migmatites, pegmatites and locally ultramafic rocks and marbles [36,40]. Metamorphic rocks from the lower and intermediate units reached amphibolite facies conditions [24,40,47,48], achieved during crustal thickening [49] at 21–18 Ma and 26–23 Ma (Rb–Sr mica ages from the main metamorphic fabric) for the lower and intermediate units, respectively [36].

Retrograde metamorphism is marked by the development of mylonite marbles, common boudinage along a shallow-dipping foliation with NE–SW stretching lineation with a top to SW sense of shear, and widespread brittle tension gashes [36,40,48,50]. Rb–Sr (on white mica and biotite) and U–Pb (on monazite

and xenotime) dating by the above authors revealed a continuous cooling history under ductile to brittle conditions from 700 °C to 300 °C from 26 Ma to 12 Ma. The exhumation *PT* path is interpreted as the result of the progressive uplift of the metamorphic rocks during the formation of the metamorphic core complex [36,51]. The emplacement of the low-angle detachment fault in the Oligocene-Miocene is also associated with the intrusion of syntectonic plutons at the SRCC scale, where the Symvolon pluton crops out 30 km to the NW of Thassos Island [52–54] (Figure 1).

2.2. The Trikorfo Area

The study area at Trikorfo is located along the major SW-dipping low-angle normal detachment separating the lower from the intermediate unit of Thassos Island. Mica schists and paragneisses predominate and tectonically overlay the marbles of Theologos (i.e. lower unit). Muscovite, phlogopite, or two mica quartzo-feldspathic schists (mica schists or paragneisses) with plagioclase (oligoclase) porphyroblasts are the most common lithologies, locally interbedded with carbonate/dolomitic rocks towards the base and top of the formation [24]. In many occurrences, these rocks are rich in minerals from the epidote and garnet groups together with common tourmaline (schorl mainly) and opaque minerals, mostly hematite and ilmenite. Metamorphic Al-silicate minerals (kyanite, fibrolitic sillimanite, andalusite, staurolite) are also documented. These mica schists are thus likely derived from calcareous pelitic sediments [24]. Interestingly, this unit also locally presents uncommon Mn-rich mineral assemblages attributed to post-metamorphic hydrothermal recrystallization [20,24,26]. The garnet–kyanite–biotite–hematite–plagioclase ± staurolite ± sillimanite paragenesis of the mica schists, contemporaneous with the ductile fabric related to extensional deformation, has been specifically interpreted as having attained *PT* conditions of 5.5 ± 1.5 kbars and 600 ± 50 °C, without any evidence of partial melting [24]. Voudouris et al. [20] documented at the top of the formation the presence of an orthogneiss at the contact with the paragneisses/mica schists. Although not exposed, a granitoid is considered to be genetically related to the widespread Miocene gold mineralization in the area [27].

3. Materials and Methods

Representative samples of host-rocks, mineral assemblages and veins were selected for bulk rock analyses and conventional 30 µm polished sections for petrographic observations and electron probe microanalyses (EPMA). Individual kyanite crystals were prepared for bulk rock analyses (powder) and for EPMA and Laser Ablation-Inductively Coupled Plasma Mass Spectroscopy (LA-ICPMS) on 200–300 µm thick sections, and UV-visible-near infrared absorption spectroscopy on 1 mm thick sections. The metamorphic paragenesis of the dominant gneiss of the area was modeled by Perple_X for *PT* conditions estimation. This work represents a compilation of samples collected by different authors during successive field campaigns, resulting in a large variety of sample labelling. All samples come from the Trikorfo area (intermediate unit of Thassos Island) (Figure 2).

3.1. Bulk-Rock Analyses

Host-rock samples CS16_292b and CS16_297 and individual kyanite crystals were powderized so as to obtain a grain-size of about 80 µm. Kyanite crystals were cut as to not contain any apparent alteration minerals, mainly micas, and cleaned with deionized water. Bulk compositions (oxides and trace elements) were obtained by ICP-Optical Emission Spectrometry and ICP-Mass Spectrometry ($LiBO_2$ fusion) at the CRPG-CNRS laboratory (Nancy, France). Sample preparation, analytical conditions and limits of detection are given in Carignan et al. [55].

3.2. Electron Probe MicroAnalyses (EPMA)

The chemical composition of minerals (samples CS16_292b, CS297, KT01-03, KT07 and MB13) was determined using a Cameca SX100 electron microprobe analyzer (EPMA) equipped only with wavelength dispersive spectrometers at the GeoRessources laboratory (Nancy, France) operating with an emission current of 20 nA, an acceleration voltage of 15 kV, and a beam diameter of 1 µm.

The following elements, monochromators, standards, and limits of detection were used: Na (TAP, albite, 515 ppm), Si (TAP, albite, 330 ppm), Mg (TAP, olivine, 265 ppm), Al (TAP, Al_2O_3, 300 ppm), K (LPET, orthoclase, 200 ppm), Ca (PET, andradite, 370 ppm), Ti (LPET, $MnTiO_3$, 250 ppm), Mn (LIF, $MnTiO_3$, 635 ppm), Fe (LIF, Fe_2O_3, 1003 ppm). Three representative samples of blue-green-colorless, yellow and orange kyanite crystals from the same locality as the ones analyzed by bulk geochemistry were selected for EPMA (profiles) analyses and X-ray maps for the elements Al, Si, Fe, Ti and Mn. All analyses were performed with FeO and MnO and converted to Fe_2O_3 and Mn_2O_3 for epidote and andalusite group minerals and Ti-hematite.

Mineral analyses (samples Th01 to Th06) carried-out at Hamburg used a Cameca-SX 100 WDS, accelerating voltage of 20 kV, a beam current of 20 nA and counting time of 20 s. Standards used were andradite (Si, Fe and Ca), Al_2O_3 (Al), MgO (Mg), albite (Na), orthoclase (K), and $MnTiO_3$ (Ti and Mn). Corrections were made using the PAP online program [56].

3.3. Laser Ablation-Inductively Coupled Plasma Mass Spectroscopy (LA-ICPMS)

Kyanite in-situ quantitative LA-ICPMS elemental analyses were performed at GeoRessources laboratory (Nancy, France) using an Agilent 7500c quadrupole ICPMS coupled with a 193 nm GeoLas ArF Excimer laser (MicroLas, Göttingen, Germany). Laser ablation was performed continuously with a speed of 2 µm/s with a constant 5 Hz pulse frequency and a constant fluence of 4.20 J/cm^2 by focussing the beam at the sample surface, from edge to edge of the crystals, along the same profiles analyzed by EPMA. Diameter of the ablation spot was 32 µm. Helium was used as carrier gas to transport the laser-generated particles from the ablation cell to the ICPMS and argon was added as an auxiliary gas via a flow adapter before the ICP torch. Typical flow rates of 0.5 L/min for He and 1 L/min for Ar were used. EPMA analyses of Si and Al served as internal standards. The certified reference materials NIST SRM 610 and 612 (concentrations from Jochum et al. [57]) were used as external standards for calibration of all analyses; they were analyzed twice at the beginning and at the end for each kyanite sample, following a bracketing standardization procedure. ^{27}Al and ^{29}Si were measured with a dwell-time of 10 ms; the following 17 isotopes were measured with a dwell-time of 20 ms for each: ^{7}Li (limit of detection of 20 ppm), ^{23}Na (70 ppm), ^{24}Mg (1 ppm), ^{39}K (50 ppm), ^{43}Ca (6000 ppm), ^{47}Ti (20 ppm), ^{51}V (1 ppm), ^{53}Cr (15 ppm), ^{55}Mn (15 ppm), ^{57}Fe (150 ppm), ^{63}Cu (10 ppm), ^{66}Zn (10 ppm), ^{88}Sr (0.5 ppm), ^{107}Ag (2 ppm), ^{137}Ba (3 ppm), ^{197}Au (1 ppm), and ^{208}Pb (0.5 ppm). All data were reduced off-line with the limits of detection calculated using the commercial version of Iolite (Version 3.71, https://iolite-software.com) data reduction software [58] running with Igor Pro. The uncertainty is calculated for each element for each analysis as a function of the uncertainty of the reference standards, the absolute element content and the time of integration [58]. The resulting value of uncertainty is then varying for a single element between each analysis and is in the order of 10% for high concentration to 80% when the element concentration is measured close to the limit of detection.

3.4. UV-Visible-Near Infrared Absorption Spectra

UV-visible-near infrared absorption spectra were measured at room temperature using a Perkin-Elmer 1050 dual beam spectrophotometer at the Institut des Matériaux Jean Rouxel (University of Nantes, France) on blue-green (sample THA16), yellow (THA08), and orange (THA13) kyanite crystals. Spectra were acquired at a resolution of 1 nm at a rate of 120 nm/min. As our samples were significantly fractured and hence translucent but not transparent, we prepared them as 1 mm thick slices. At this thickness, they became sufficiently transparent so that the light beam could go through, and they also remained colored enough to characterize spectral features related to color.

3.5. Phase Diagram Calculation

PT conditions of the main paragneiss host-rock (sample CS16_292b) were modeled on the basis of the paragenesis described in Section 4.2. The phase diagram was calculated using Perple_X Version 6.8.5 (http://www.perplex.ethz.ch) [59] and the internally consistent end-member data set of Holland

and Powell [60]. Calculations were undertaken in a set of chemical systems ranging from NCKFMASH to MnNCKFMASHT(O) ($MnO–Na_2O–CaO–K_2O–FeO–MgO–Al_2O_3–SiO_2–H_2O–TiO_2–O_2$) in order to constrain the effect of TiO_2, Fe_2O_3 and MnO-bearing minerals.

Phases involved in modeling are biotite (Bt), chlorite (Chl), cordierite (Crd), epidote (Ep), garnet (Gt), ilmenite (Ilm), kyanite (Ky), melt (L), plagioclase (Pl), quartz (Qtz), rutile (Rt), sillimanite (Sil), staurolite (St) and white mica (Ms). The solution models utilized for metamorphic minerals and the bulk rock composition are presented in the Table 1 and Table S1, respectively. We used the Ilm(WPH) solution model which enables the calculation of hematite, geikielite and ilmenite end-member abundance [61]. Water was assumed to be saturated.

Table 1. Solution models used for the pseudo-sections (See Figure 15a). See Perple_X documentation (http://www.perplex.ethz.ch) for detailed information.

Phase	Solution Model Label in Perple_X	References
Biotite	Bi(W)	[62]
Chlorite	Chl(W)	[62]
Chloritoid	Ctd(W)	[62]
Cordierite	Crd(W)	[62]
Garnet	Gt(W)	[62]
Ilmenite	Ilm(WPH)	[62]
Melt	melt(W)	[62]
Orthopyroxene	Opx(W)	[62]
Plagioclase	Pl(h)	[63]
Staurolite	St(W)	[62]
White mica	Mica(W)	[62]

4. Results

4.1. Tectonic and Structural Setting of Al-Silicates

The main lithology of the Trikorfo area is dominated by garnet–kyanite–biotite–hematite–plagioclase ± staurolite ± sillimanite bearing paragneisses/mica schists. At the scale of Thassos Island, the orientation of the main foliation varies widely due to post-foliation tectonic events, including large-scale folding. In the Trikorfo area, rare relics of an early foliation S_{n-1} are observed. The paragneisses/mica schists mainly show a sub-horizontal (azimuth N140-300, dip up to 20° W) S_n foliation, bearing kyanite mineral lineation, oriented N255 ± 15°, and gently dipping to the WSW. Late brittle deformation is evidenced by tension gashes that cross-cut S_n. These veins are oriented N330 ± 15° and are generally close to vertical. The variation in the orientation of the tension gashes is the same as the regional lineation underlined by synmetamorphic kyanite crystals within 30° that may reflect their continuous formation during counter-clockwise rotation of Thassos Island [40].

4.2. Lithological Units and Rock Sampling

Samples CS16_292b (Figure 3a) and CS16_292a represent the main paragneiss/schist host-rock, apparently unaltered at the outcrop scale. An increasing number of green layers parallel to the gneiss foliation are observed towards the top of the formation (samples CS16_297 (Figure 3b) and Th06). Although not analyzed in our samples, the presence of braunite in the mica schists of the Trikorfo area was shown by previous studies [26,28]. Green to red calc-silicate rocks (up to 80 cm wide) are observed, at the top of the formation, interbedded or at the contacts between quartzo-feldspathic mica schists and metacarbonate rocks (Figure 3c). The rocks typically show a mineral zonation with tremolitic hornblende, diopside, quartz, anorthite/bytownite, epidote, grossular, titanite and Mn-bearing clinozoisite from an outer band adjacent to host mica schists towards the center of the layer (samples Th01, Th02, Th03, KT01 and KT02 (Figure 3c–e)). Sample Th04 is a spessartine–epidote–braunite–hornblende mica schist.

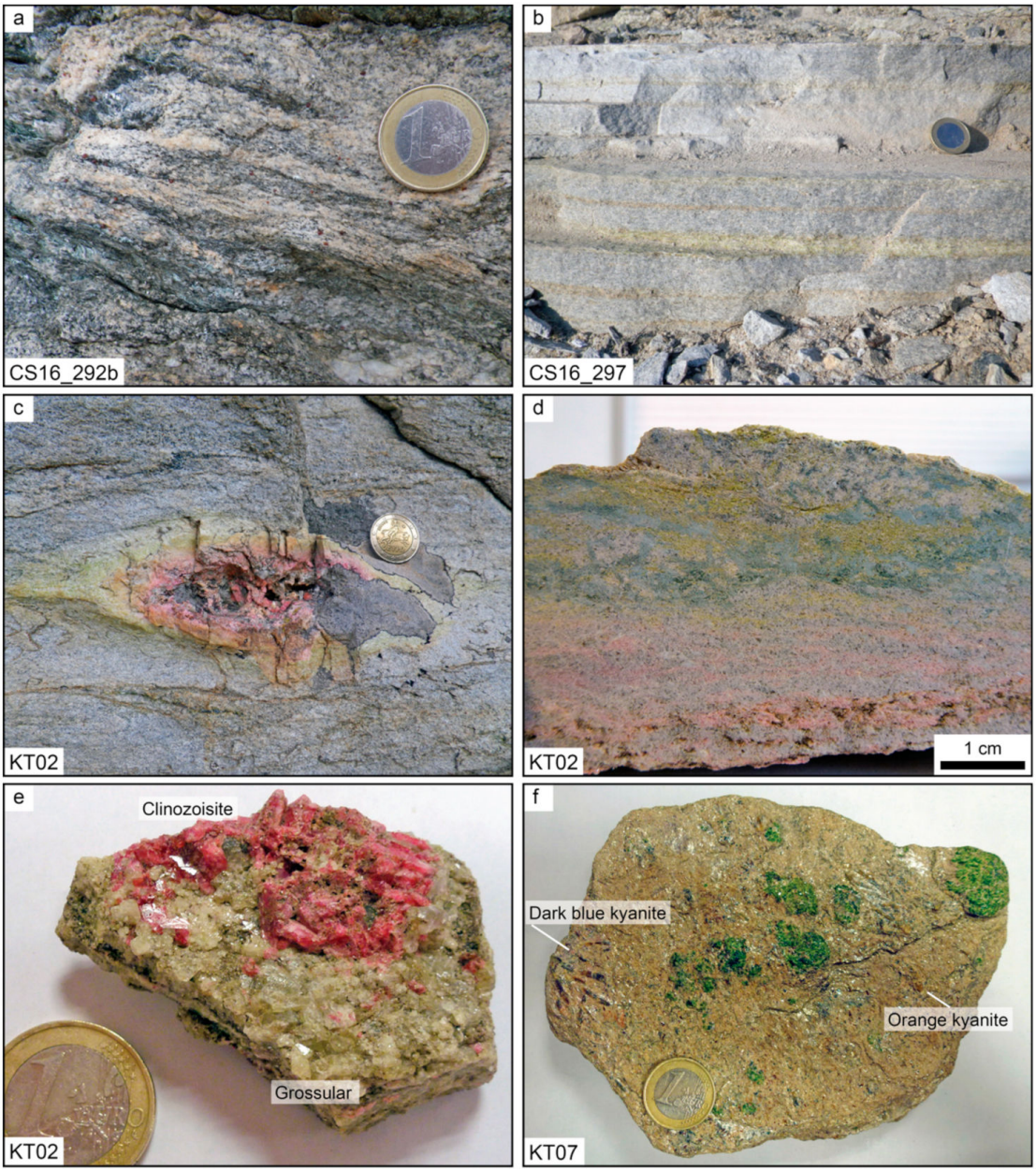

Figure 3. (**a**) Main garnet–kyanite–biotite–hematite–plagioclase ± staurolite ± sillimanite bearing gneiss of the Trikorfo area (sample CS16_292b, N290/65N). (**b**) Green epidote-rich horizon parallel to the main gneiss foliation (sample CS16_297, N270/11N). (**c**) Lense slightly oblique to the subhorizontal gneiss foliation showing a zonation of green epidote and pink clinozoisite together with grossular in a geode (sample KT02). (**d**) Mineralogical zonation with diopside, hornblende, epidote (green), grossular and clinozoisite (pink-red), sample KT02 equivalent to Th04. (**e**) Close up to the core of the geode to near gem-quality pink clinozoisite (clinothulite) and grossular association within locality sample KT02. (**f**) Deep green Mn-rich andalusite (viridine) and kyanite (deep blue and orange) association in sample KT07.

Kyanite is found as a metamorphic mineral, underlining the mineral lineation of the main paragneisses/mica schists rocks as in sample CS16_292b. Locally at the top of the formation, kyanite–piemontite ± andalusite ± muscovite ± spessartine ± braunite mica schists (where kyanite is distributed without any specific orientation) are intercalated within the spessartine–kyanite-bearing mica schists (samples Th05, KT03 (Figure 4a), KT05, and KT07 (Figure 3f)).

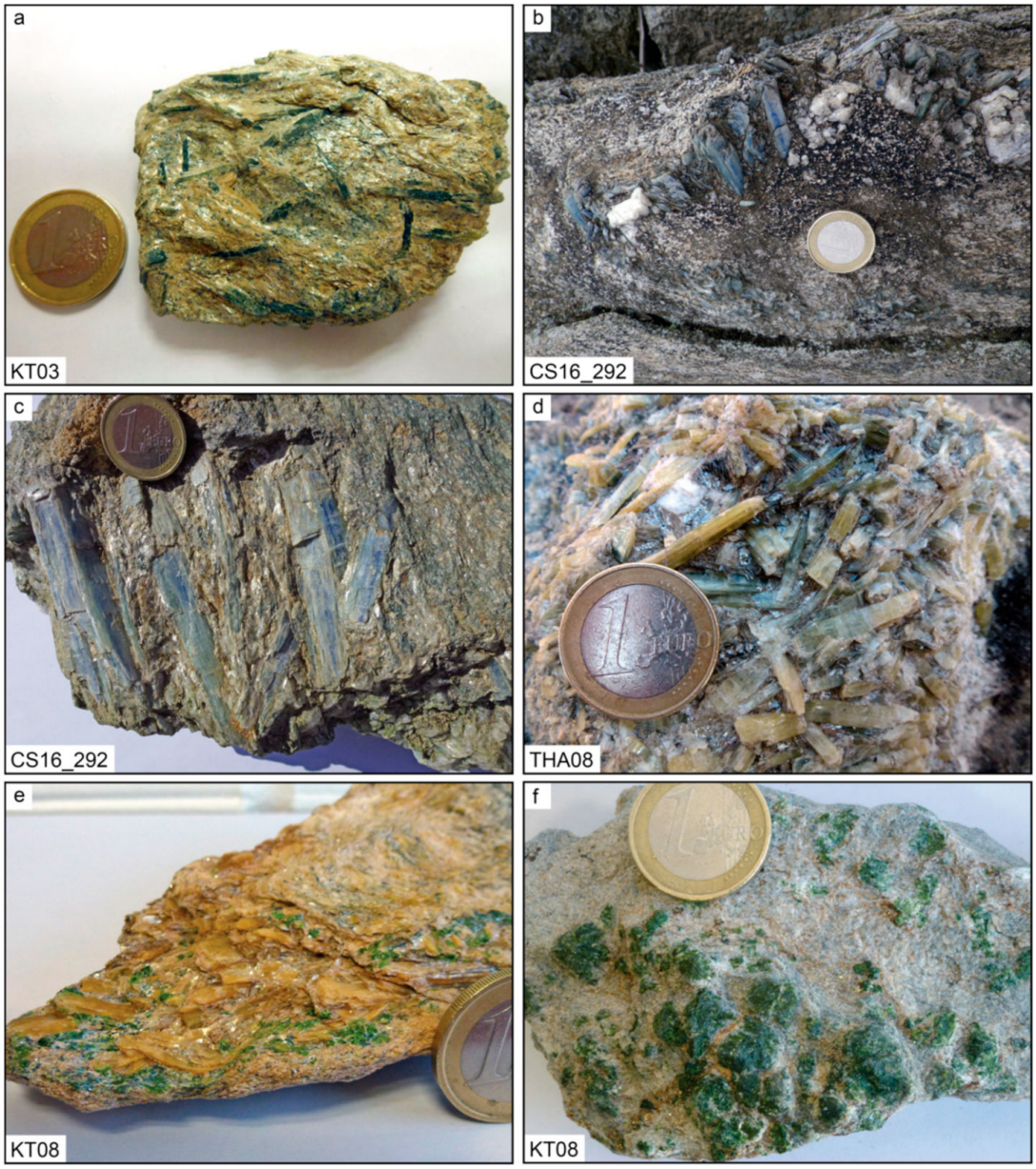

Figure 4. Different kyanite color types encountered in the Trikorfo area (Thassos Island). (**a**) Unoriented dark blue kyanite in a mica schist collected towards the top of the area. (**b**) Zoned blue (core) to green-transparent (rim) kyanite in a deformed and folded quartz vein. The pluricentimetric kyanite crystals are found at the interface between the gneiss and the vein. The crystals are weakly deformed and generally oriented parallel to the rock lineation. (**c**) Close-up on zoned-blue kyanite mostly aligned parallel to the rock foliation. (**d**) Field photograph of zoned dark blue-yellow isotropically distributed kyanite crystals in a quartz vein. (**e**) Orange kyanite crystals, generally oriented parallel to gneiss lineation, associated with green Mn-rich andalusite (viridine) and quartz. (**f**) Aggregate of centimetric green Mn-bearing andalusite crystals.

Towards the top of the formation, pluricentimetric kyanite crystals are observed at the contact between metamorphic quartzo-feldspathic kyanite-bearing rocks and coarse-grained quartz-feldspar veins, which are transposed within or secant to the main foliation. In this case, kyanite is generally weakly oriented parallel to the regional lineation. In general the crystals are zoned with dark blue cores and green-transparent (Figure 4b,c) to yellow rims (Figure 4d). Less common are orange kyanite-bearing samples showing association with green andalusite, spessartine and piemontite (Figure 4e,f).

An orthogneiss exposed in the area is composed of orthoclase, oligoclase/andesine along with phlogopite, quartz, hematite, epidote and allanite and is surrounded by a transitional zone with the same mineralogy as the above mentioned calc-silicate layers (i.e. amphibole, plagioclase, and epidote mineral groups from granitoid outwards) [20]. The presence of pluricentimetric crystals of tourmaline (schorl mainly) was also shown in quartz veins and late brittle fissures [20].

Late brittle veins cross-cutting the metamorphic foliation are dominated by euhedral quartz, clinochlore, ilmenite, albite and adularia [20]. Rare veins are enriched in Mn as evidenced by centimetric euhedral crystals of spessartine (Sample MB13; Figure 5).

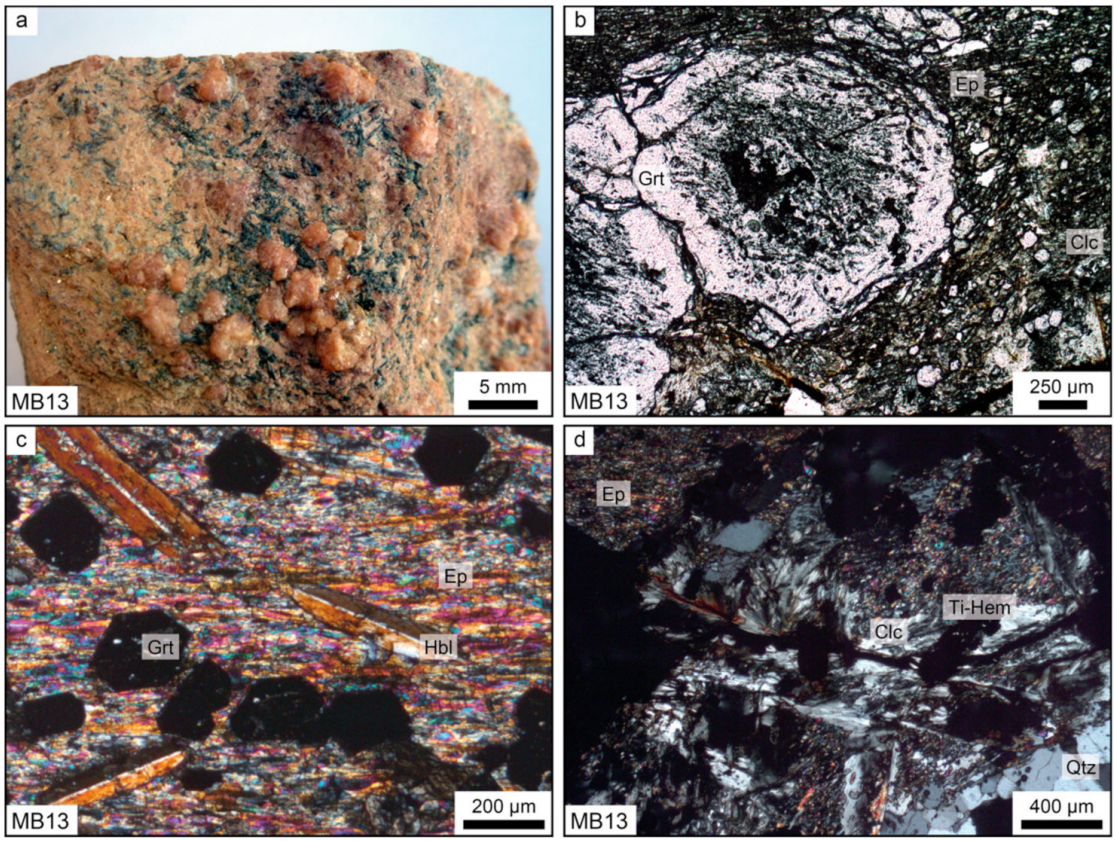

Figure 5. Late brittle fracture sample MB13. (**a**) Hand specimen showing mainly spessartine (orange), Mn-bearing clinochlore and hornblende (green) and quartz. (**b**) Plane polarized light (PPL) photomicrograph with euhedral spessartine (Grt), Mn-rich epidote (Ep) and Mn-bearing clinochlore (Clc) assemblage. (**c**) Crossed-polarized light (XPL) photomicrograph with secondary spessartine (Grt) and hornblende (Hbl) overprinting the metamorphic foliation underlined by Mn-rich epidote (Ep). (**d**) XPL photomicrograph showing Mn-rich epidote (Ep), Mn-bearing clinochlore (Clc), Ti-hematite (Ti-Hem) and quartz (Qtz) association.

4.3. Mineralogy and Mineral Chemistry of Paragneisses/Mica Schists of the Metamorphic Unit at Trikorfo

The composition of two host-rock samples (CS16_292a and _292b) is shown in Table S1a. The structure of the rock is granolepidoblastic with quartz-plagioclase-dominated layers and a schistosity underlined by biotite locally retrogressed to chlorite. C′/S structures indicate top N228 sense of shear. The mineralogy is made of biotite, garnet, quartz, kyanite, staurolite, plagioclase, apatite and Ti-hematite (Figure 6a). Rare late muscovite and epidote are observed without any preferential orientation (Figure 6a).

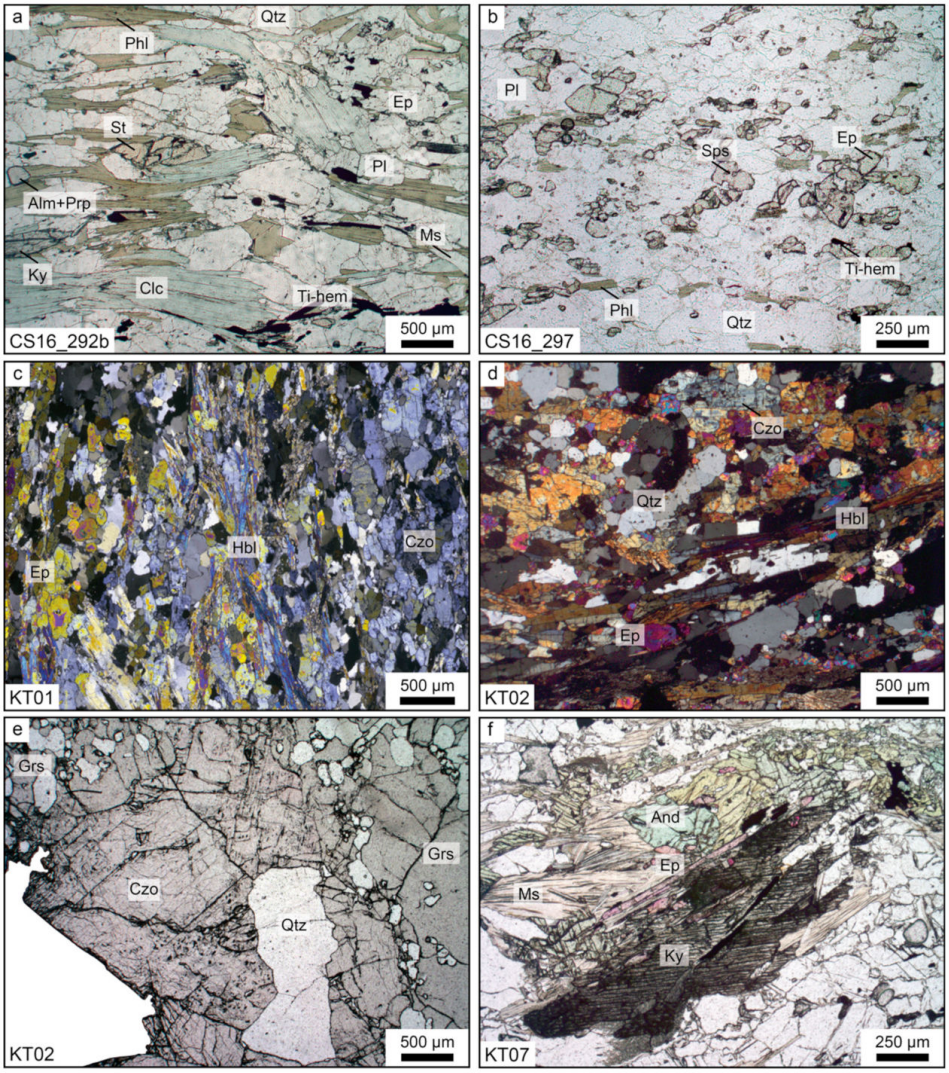

Figure 6. Main mineralogical assemblages from the Trikorfo area. (**a**) Biotite–garnet–kyanite–staurolite–plagioclase-quartz–Ti–hematite paragenesis of the main paragneiss unit modeled with Perple_X. Chlorite (clinochlore/amesite) is a retrogressed phase of phlogopite. Scarce late muscovite and epidote are observed. (**b**) Phlogopite–spessartine–epidote association of the quartz-dominated green horizon parallel to the gneiss foliation. (**c**) Clinozoisite and epidote layers and secondary amphibole in sample KT01 under XPL. (**d**) Clinozoisite–epidote–hornblende in sample KT02 under XPL. (**e**) Grossular-quartz–clinozoisite (clinothulite) microscopic view (PPL) of sample KT02. (**f**) Secondary Mn-rich epidote, orange kyanite and green andalusite assemblage of sample KT07 under PPL. Mineral abbreviation: Almandine + pyrope (Alm + Prp), Andalusite (And), Clinochlore/amesite (Clc), Clinozoisite (Czo), Epidote (Ep), Grossular (Grs), Hornblende (Hbl), Kyanite (Ky), Muscovite (Ms), Phlogopite (Phl), Plagioclase (Pl), Quartz (Qtz), Staurolite (St) and Ti-hematite (Ti-Hem).

Biotite has the composition of phlogopite with X_{Mg} in the range 0.73–0.75 (Table S2a). Plagioclase is oligoclase/andesine with a composition between An_{23} and An_{34} (Table S3a). Garnet and staurolite crystals are isolated in the mica-rich layers. Garnet grains are always corroded remnants of preexisting porphyroblasts (Figure 6a). Garnet chemistry (Table S4a) is dominated by X_{Fe} (up to 39.25) and X_{Mn} (up to 44.06); X_{Mg} is significant, up to 18.82, and X_{Ca} is never higher than 7.72. Garnet composition thus lies close to the border between almandine-(pyrope) and spessartine fields (Figure 7a). No significant and systematic chemical variation was noticed from border to border among all analyzed crystals (Table S4a). Staurolite, also corroded, contains significant amounts of MnO, up to 1.47 wt. % (Table S5). Although Dimitriadis [24] indicated that kyanite seems to postdate garnet growth (no kyanite inclusions in

garnet and garnet early porphyroblast remnants might be enveloped by kyanite crystals), the relations are not so clear in sample CS16_292b because most of the crystals are isolated from each other. Our observations did not provide convincing evidence that kyanite postdates garnet growth and both minerals are thus considered as cogenetic. Fe-rich (up to 1.23 wt. % FeO) syn-metamorphic kyanite crystals are oriented parallel to the main foliation S_n. Chlorite analyses revealed a composition between clinochlore and amesite (Figure A1; Table S11). All opaque minerals analyzed by EPMA were Ti-rich hematite (Table S6a). Rare ilmenite was identified by optical microscopy.

4.4. Mineralogy and Mineral Chemistry of Green-Colored Horizons

Sample CS16_297 is representative of the many green-colored horizons parallel to the foliation of the main schist/paragneiss unit of the Trikorfo area (Figure 3b). Element analyses are reported in Table S1a. The structure is mainly granoblastic with the Sn foliation locally underlined by phlogopite alignment. Identified minerals include biotite, quartz, plagioclase, garnet, epidote, Ti-hematite, titanite, rutile and apatite (Figure 6b). Magnetite with hematite exsolution was noticed. The mineralogy is dominated by quartz with layers rich in secondary spessartine and/or epidote/clinozoisite. Biotite has the composition of phlogopite with X_{Mg} in the range 0.72–0.74 (Table S2b). Plagioclase is oligoclase with a composition of An_{15} to An_{21}, slightly depleted in CaO compared to CS16_292b (Table S3b). The content of TiO_2 in Ti-hematite does not exceed 8.15 wt. % (Table S6b). The composition of titanite and rutile is given in Table S9a. Chlorite, staurolite, kyanite and sillimanite are not found in this rock.

The shape of garnet crystals is usually irregular. X_{Fe} and X_{Mg} are much lower (up to 21.69 and 3.24, respectively), and X_{Mn} and X_{Ca} (up to 58.00 and 37.29, respectively) significantly higher than garnet from sample CS16_292b. No significant and systematic chemical variation was noticed from border to border among all analyzed crystals (Table S4b) and garnet composition falls in the spessartine field (Figure 7a). Epidote is abundant and shows a composition depleted in Mn^{3+} ranging from epidote end-member to Fe^{3+}-rich clinozoisite (Figure 7b; Table S7a,j) and is responsible for the green coloration within these rocks.

4.5. Mineralogy and Mineral Chemistry of Calc-Silicate-Dominated Horizons

Moving towards the top of the formation, the thickness of the green layers increases and green-red horizons up to 80 cm thick are visible (Figure 3c,d). These beds are intercalated within the main foliation of the kyanite-bearing paragneisses/mica schists at proximity of carbonate/dolomitic rocks. They typically show calc-silicate assemblages more or less enriched in Mg- and Mn-bearing minerals with typical mineralogical zonation showing tremolitic hornblende, diopside, quartz, anorthite/bytownite, clinozoisite/epidote, grossular, titanite and pink clinozoisite from an outer band adjacent to host mica schists towards the center of the layer (Figure 3c,d) [20,24].

The dark green external part of the calc-silicate is dominated by Mn-bearing varieties of diopside (up to 1.44 wt. % MnO) and hornblende (up to 2.75 wt. % MnO) (Table S8a,c,d). The progressive change in color from pale green to red (samples KT01-02, Th01-03) is mainly due to variation in epidote composition, whose EPMA analyses are presented in Table S7b,e–g, and reported in the Mn–Al–Fe ternary plot of Figure 7b.

Green epidote is reported in green layers parallel to rock foliation as in sample CS16_297 previously described and at the outer margins of the calc-silicate layers along with hornblende, anorthite/bytownite (Table S3d) and titanite (Table S9b) (Figure 6c,d). The composition evolves from epidote to clinozoisite end-members (Figure 7b). It may contain up to 1.04 wt. % MnO. LREE were not analyzed for epidote mineral group; their presence may mark the low total of some of the analyses.

Mn-poor clinozoisite exhibits subhedral to euhedral crystals. The pale pink crystals are usually found in the intermediate zone of the calc-silicate layers mostly associated with quartz, anorthite, titanite, diopside and hornblende. Available microprobe data revealed Fe_2O_3 content between 1.36 and 6.11 wt. % (sample KT02) and between 1.54 and 11.06 wt. % (samples Th01 and Th03), and minor Mn_2O_3 content below 0.67 wt. % (Table S7b,e,g).

Near gem-quality Mn-poor clinozoisite, with the same optical and chemical properties as clinothulite variety described by Bocchio et al. [64], is locally observed in the inner part of the calc-silicate layers, intergrown with Mn-grossular, titanite and quartz, both in the matrix of the rock and in fissures cross-cutting the foliation. The crystals occur in deep pink to red colors and form translucent subhedral to euhedral crystals up to 10 cm (Figures 3e and 6e; Table S7b,f). EPMA data revealed low contents of Fe_2O_3 (<3.15 wt. % in sample KT02 and <2.90 wt. %, in sample Th02) and Mn_2O_3 (<0.72 wt. % in sample KT02 and <0.21 wt. % in sample Th02), however high enough to be responsible for the pink-red coloration.

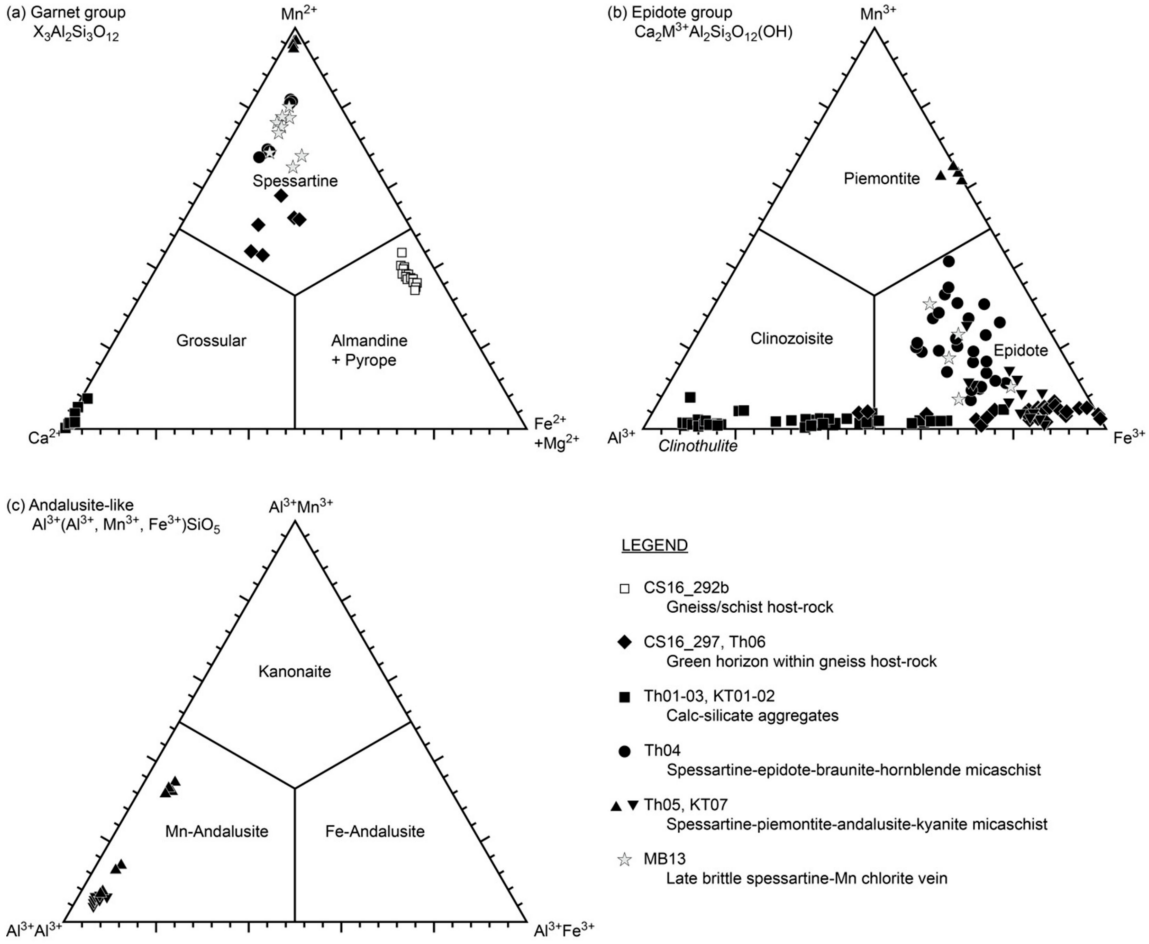

Figure 7. Ternary plots showing compositions of the garnet, epidote and andalusite group minerals. (**a**) Garnet composition considering spessartine, grossular and almandine + pyrope end-members. Garnet composition is $X_3Al_2Si_3O_{12}$ with the X site occupied by divalent cations, Mn^{2+} for spessartine, Ca^{2+} for grossular, Fe^{2+} for almandine and Mg^{2+} for pyrope, e.g., [65]. (**b**) Epidote group minerals, $Ca_2M^{3+}Al_2Si_3O_{12}(OH)$, classified according to one M^{3+} cation substitution with Al in octahedral coordination with M^{3+} = Al^{3+}, Mn^{3+} or Fe^{3+}, corresponding to the clinozoisite, piemontite and epidote end-members, respectively [66,67]. Composition analyses for deep pink to red clinozoisite (clinothulite) are shown. (**c**) Andalusite-like minerals, $Al^{3+}(Al^{3+}Mn^{3+}Fe^{3+})SiO_5$, classified according to octahedral Al substitution with Mn^{3+} or Fe^{3+} [2,68].

In the calc-silicate lenses, pure grossular to Mn-bearing grossular form euhedral yellowish crystals of near gem-quality in close association with pink to red colored Mn-bearing clinozoisite and quartz (Figures 3e and 6e). MnO content ranges from 0.08 to 3.60 wt. % (Table S4c,e). All data are plotted in the ternary Mn–Ca–Fe + Mg diagram (Figure 7a).

4.6. Mineralogy and Mineral Chemistry of Mn-rich Schist Layers and Quartz Lenses

Near the top of the Trikorfo area, the formation is dominated by schist layers (samples Th04, Th05 and KT07) and intercalations of quartz lenses (sample KT08) particularly enriched in Mn-bearing minerals as shown by the assemblage of piemontite and Mn-rich epidote together with Mn-rich andalusite and spessartine (Figures 3f, 4d and 5f). Although EPMA analyses were not entirely satisfying (MnO between 27.99 and 45.31 wt. % and maximum total of all analyzed elements of 51.80 wt. %), probably reflecting the heterogeneity and variable Mn oxidation state of the minerals, Mn-oxides could be identified (Table S10). In both lithologies, piemontite and Mn-rich epidote form dark pink/purple-colored prismatic crystals with typical piemontite pleochroism. Microprobe analyses revealed piemontite in the andalusite-bearing mica schists with Mn_2O_3 content up to 12.69 wt. % and Mn-rich epidote in association within the spessartine–braunite–quartz aggregates with Mn_2O_3 in the range of 0.13 to 6.59 wt. % (Figure 7b, Table S7c,h,i). Phlogopite has X_{Mg} of 0.96–0.97 (Table S2d). Plagioclase is oligoclase/andesine with a composition between An_{22} and An_{34} (Table S3c).

Garnet is also marked by enrichment in Mn (Figure 7a). Translucent, orange, euhedral crystals of spessartine up to 1 cm are found (i) in intercalated spessartine–epidote–braunite–hornblende mica schists, and (ii) in spessartine–piemontite–andalusite–kyanite mica schists. Within the spessartine–epidote–braunite–hornblende mica schists, spessartine commonly forms large euhedral crystals with numerous inclusions of epidote and is surrounded by epidote and magnesio–hornblende. Spessartine from the spessartine–piemontite–andalusite–kyanite mica schists is also associated with muscovite, phlogopite, anorthite and hematite. Electron microprobe analyses of spessartine indicate X_{Mn} in the range 64.74–97.19 (Table S4e).

A late brittle vein cross-cutting the Mn-rich schist layers was sampled (MB13; Figure 5). Up to 1 cm near gem-quality euhedral crystals of spessartine (X_{Mn} of 81.23; Figure 7a; Table S4d) are observed together with quartz, Mn-rich epidote (up to 6.67 wt. % Mn_2O_3; Figure 7b; Table S7d), Mn-bearing clinochlore (up to 1.64 wt. % MnO; Figure A1; Table S11d), Mn-bearing hornblende (up to 1.99 wt. % MnO; Table S8b) and almost pure hematite (Table S6c).

Accessory phases include monazite (relatively abundant in discrete layers), titanite and zircon. Tourmaline is very abundant in quartz lenses within mica schists, where it occurs as black crystals (schorl) up to 10 cm and associated with muscovite and chlorite (clinochlore). However not analyzed, olive green-colored tourmaline (crystals up to 3 cm) is observed. Tourmaline is also present in fissures intergrown with clinochlore, titanite and quartz. Finally, up to 10 cm tremolite white crystals were documented in sheared marbles [20].

4.7. Mineralogy and Mineral Chemistry of Kyanite–Quartz Veins

4.7.1. Different Colors of Kyanite Crystals

Among the many spectacular minerals observed at the Trikorfo area, kyanite, found at the contact between quartzo-feldspathic coarse-grained veins and the paragneiss/mica schist rocks, towards the top of the series, is of particular interest. The crystals show a general orientation parallel to the regional foliation but may also be unoriented (Figure 4a). The up to 20 cm crystals are slightly bent as a result of weak plastic deformation. Over a small area of a few km^2, besides the Fe-rich syn-metamorphic kyanite already described in the metamorphic paragenesis (Table S12a), we report at least four dominant types of kyanite based on their color: (i) dark blue-black (Figure 4a, Table S12b), (ii) zoned crystals with dark blue cores and transparent-green rims (Figure 4b,c), (iii) zoned crystals with dark blue cores and yellow rims (Figure 4d) and (iv) orange crystals generally associated with green Mn-rich andalusite (Figure 4e; Table S12c). Most of the crystals are inappropriate for faceting as marketable gemstones due to common fractures, but are at least proper for cabochon-shaped material. In addition, with regard to their overall aesthetic aspect, mainly large size and vivid color, these kyanite crystals are referred to as being of near gem-quality.

4.7.2. Bulk Element Concentration of Individual Kyanite Crystals

When observed down their <100> faces, most kyanite crystals show blue-green-colorless bands parallel to the *c*-axis. Representative kyanite samples have been selected for bulk element concentration analyses (zoned kyanite THA16_1, _2, _3, yellow THA08, pale orange THA12 and deep orange THA13; Figure 8). The elements are classified as oxides and trace elements according to their content in the host rock sample CS16_292b (* symbol in Figures 9a, 10 and 11).

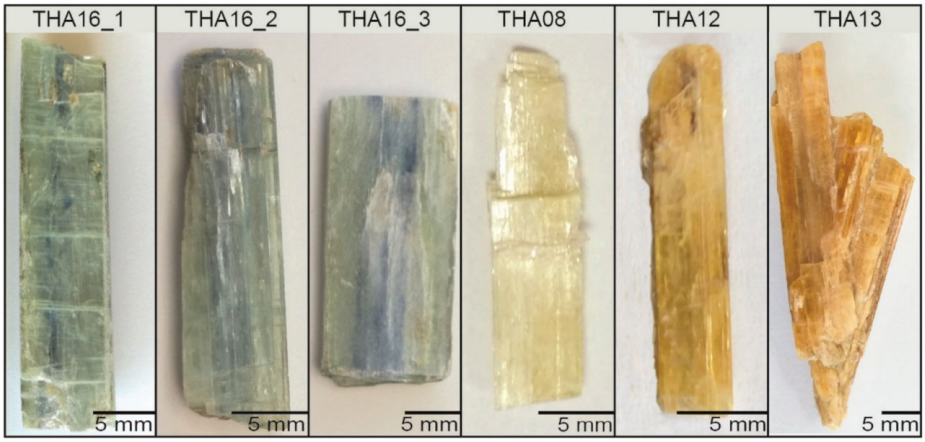

Figure 8. Photographs of individual kyanite crystals prior to bulk rock analyses.

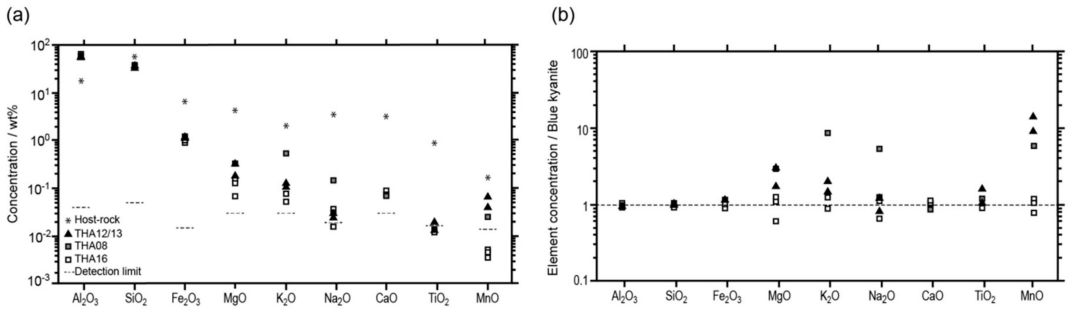

Figure 9. Distribution of measured oxides in CS16_292b host-rock and in blue-green (THA16), yellow (THA08) and orange (THA12 and THA13) kyanite samples. (**a**) Raw concentration. (**b**) Concentration normalized to the average value of the three blue-green THA16 samples.

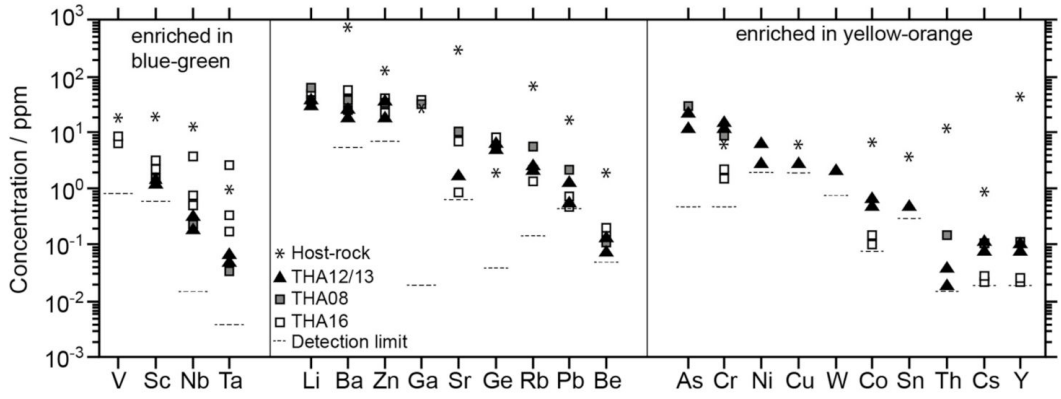

Figure 10. Trace element composition of host-rock CS16_292b and kyanite samples ordered by decreasing concentration. The left part shows elements which are preferentially found in blue-green THA16 kyanite samples, the central part where there is no significant difference among the samples and the right part reports the elements with significant enrichment in yellow THA08 and orange THA12/13 kyanite samples.

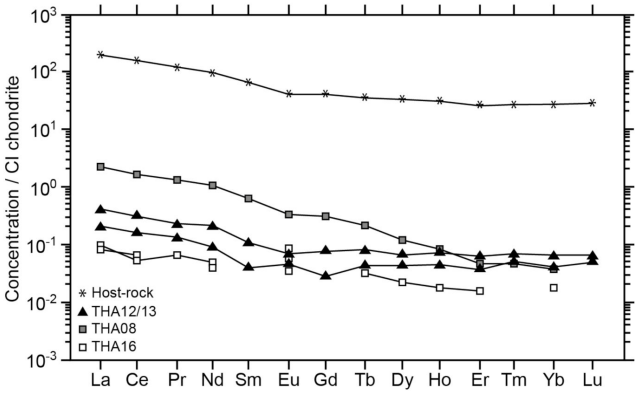

Figure 11. REE spider diagram of blue-green (THA16), yellow (THA08) and orange (THA12 and THA13) kyanite individual crystals and of the host rock sample CS16_292b. The normalizing factors are related to CI chondrite values [69].

The amount of Al_2O_3 and SiO_2 is comparable between all analyzed kyanite samples, higher than 96 wt. % Al_2SiO_5. The measured oxides show a decreasing concentration from Fe_2O_3, MgO, K_2O, Na_2O, CaO, MnO and TiO_2 (Figure 9a). These elements generally show a preferential enrichment in the orange kyanite (Figure 9b), except Na_2O, K_2O, CaO and LOI content (Table S1b), which appear to be correlated but randomly distributed between the samples. This is likely due to alteration phases in microfissures. The total amount of Fe_2O_3, MgO, MnO and TiO_2 increases with coloration from blue-green (1.10–1.21 wt. %), to yellow (1.51 wt. %) and orange (1.42–1.61 wt. %). Yellow and orange samples show markedly higher amounts of MnO (up to one order of magnitude) and MgO (Figure 9b).

Minor elements from the bulk rock analyses are found with amounts lower than 100 ppm in kyanite samples. Ba, Zn and Ga are the most abundant elements. Blue-green kyanite is significantly enriched in V, Nb, Sc and Ta. Yellow and orange samples of kyanite contain predominant amounts of As, Cr, Ni, Cu, W, Co, Sn, Th, Cs and Y. For all other trace element contents, there is no significant difference among the analyzed samples (Figure 10; Table S1c).

The rare earth element concentration measured in each sample was normalized to chondritic abundance (Figure 11). All kyanite samples have comparable chondrite-normalized REE patterns as CS16_292b host-rock with a slight decrease until Gd and then relatively flat towards heavy REE. As for all other elements, REE are less abundant in blue-green samples than in yellow and orange kyanite. The yellow (THA08) sample is characterized by a remarkable enrichment in light REE compared to other samples. This is to be correlated with the higher content of this sample with the elements attributed to alteration phases in microfissures such as K, Na, Li, Sr and Ba.

4.7.3. EPMA X-ray Maps and Element Distribution

For all the samples, Al and Si variations are difficult to interpret. Both elements appear relatively homogeneous throughout the crystals and their maximum/minimum concentration seems to be slightly anti-correlated, likely due to a problem of surface homogeneity. A decrease of Al is noticed on the edges of THA16 marking alteration or re-equilibration with minerals in the surrounding rock. The element Mn also does not show any obvious variation in the different analyzed areas. The only point of interest regarding Mn is that, accordingly with bulk rock analyses, the concentration is lower in blue THA16 (<0.10 wt. % MnO) than in the yellow THA08 (<0.18 wt. % MnO) and orange THA13 (<0.16 wt. % MnO) kyanite samples.

Fe concentration however shows very contrasting behavior. In kyanite samples THA16 (<1.27 wt. % FeO) and THA08 (<1.59 wt. % FeO), the variations are straight and parallel to the *c*-axis. At this scale, the higher concentration seems to be correlated with the clearer parts of the kyanite crystals. In sample THA13 (<1.56 wt. % FeO), Fe distribution seems to be oblique regarding the orientation of the *c*-axis and could be related to plastic deformation of the analyzed crystal (Figure 12).

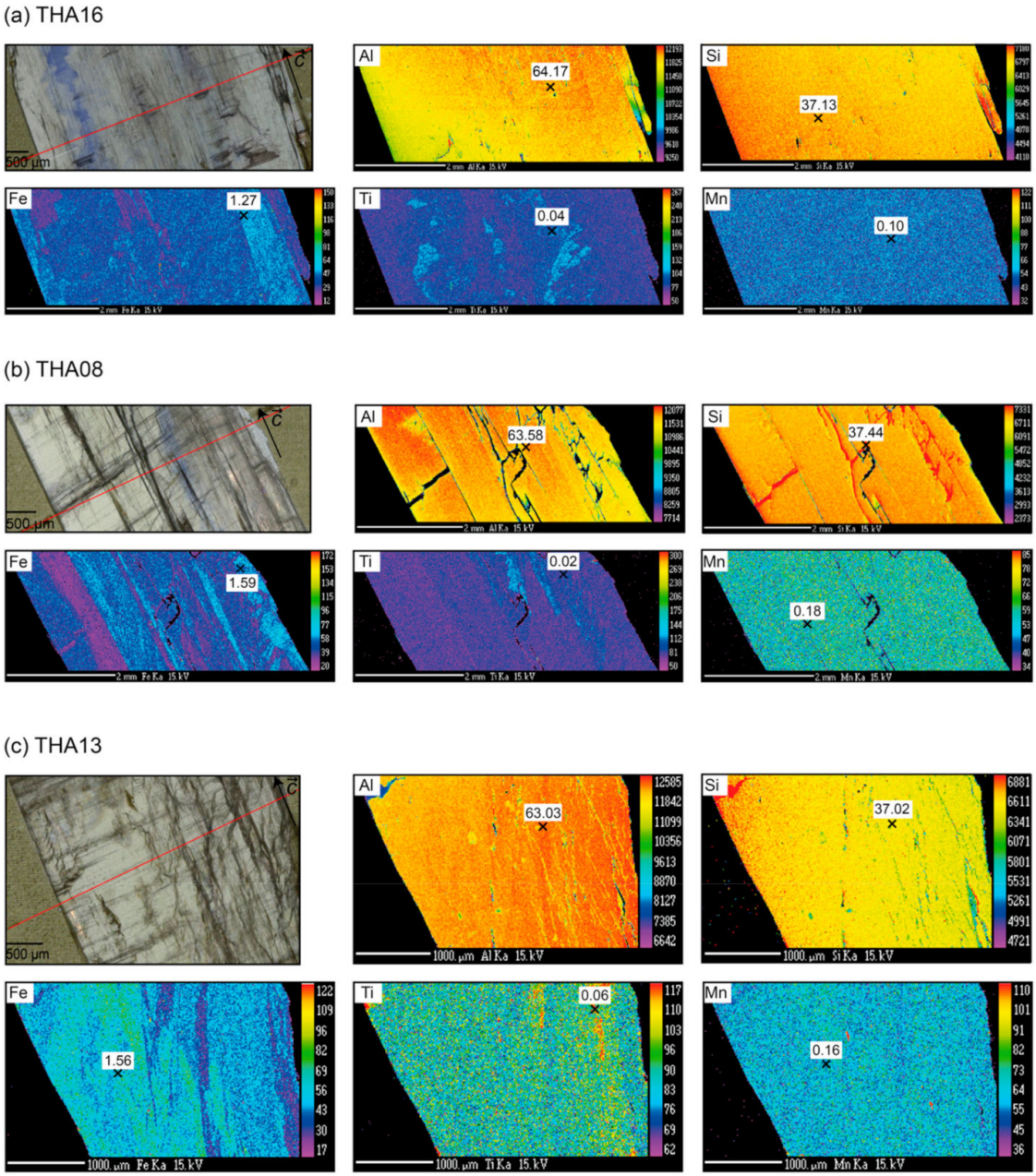

Figure 12. Electron probe microanalyses (EPMA) semi-quantitative X-ray maps of Al, Si, Fe, Ti and Mn on the <100> faces of blue-green THA16 (**a**), yellow THA08 (**b**) and orange THA13 (**c**) kyanite samples, with color scales expressed in counts, not calculated to concentration. The red line corresponds to the EPMA quantitative profile analyses (Table S12d–f). The maximum values (in oxide wt. %) measured along the profile for a given element is reported on each map.

Ti distribution is discontinuous and does not seem to be related with crystallographic orientation. Three marked areas of higher concentration are highlighted in THA16 (<0.05 wt. % TiO_2) and seem to correspond to the blue area of the crystal, at least for the left one. It is also the case to the right of the crystal, but the blue coloration is barely visible. The direct correspondence between blue coloration and Ti concentration is however difficult to establish firmly as most of the blue area is below the sample surface. In sample THA08 (<0.02 wt. % TiO_2) also, the irregular distribution of Ti reveals enrichment at the central right part of the crystal where a thin blue zonation is observed. On THA13 (<0.06 wt. % TiO_2), Ti distribution follows that of Fe, though anti-correlated.

4.7.4. Orange Kyanite and Green Andalusite Assemblages

This atypical polymorphic association is observed towards the top of the formation (i) in kyanite–phlogopite–piemontite–quartz–plagioclase ± muscovite ± spessartine ± braunite mica schists, and (ii) in quartz-feldspar-muscovite lenses. Mn-rich andalusite forms dark green-colored subhedral to euhedral crystals up to 7 cm. In both cases, kyanite and andalusite seem to have grown at equilibrium (Figure 6f). Green andalusite is commonly zoned likely due to twinning, and exhibits deformation lamellae [29]). EPMA data reveal elevated Mn_2O_3 contents, up to 15.98 wt. % (Figure 7c; Table S13a,b).

4.7.5. LA-ICPMS Profiles

The limits of detection of LA-ICMPS are significantly lower than those of EPMA and many elements can be analyzed sequentially during the same analytical run. Edge to edge sections were conducted at the same position, or approximately, as that for the EPMA profiles on the three kyanite samples (Figure 13). Al and Si variations serve as internal standards to provide quantitative elemental evolution through kyanite and are not reported on the figures. All analyses of Ca, Cu, Ag and Au were below the limits of detection. For each sample, the elements are reported according to three different groups with (i) the dominating elements (Fe, Mn, Ti, Mg and Zn) on top, (ii) the elements generally enriched in alteration minerals (K, Na, Li, Sr and Ba) in the middle, and (iii) the other elements, mainly transition metals, only found as traces in the host-rock (Cr, Pb and V) on the lower part.

Kyanite sample THA08 shows large variations in the concentration of the elements K, Na, Li, Sr and Ba. Moreover, it can be noticed that these elements are mainly concentrated either on the sides of the crystals or along fractures inside the crystals, which are common in THA08. Accordingly, these elements are interpreted as the result of alteration or late equilibration with host-rock minerals (feldspars and micas like muscovite and phlogopite).

In all samples, Fe is by far the most common element besides Al and Si. Local concentration decreases are observed where the amount of alteration elements increases, as is clearly visible on sample THA08. Mn and Ti are in the same order of magnitude in THA16 and THA08 but with Ti slightly higher in the blue-green kyanite. Mn concentration does not correlate with any color change, whereas that of Ti shows a relatively good correspondence with the blue color bands, even if they are below the sample surface. This is especially well expressed in THA08 where Ti > Mn at the intersection with the blue band. It is also visible on THA16, where the three Ti highs seen in the EPMA mapping are distinguishable, and correspond to a blue color on the left. However, it must be kept in mind that blue color is mostly below the crystal surfaces. Also, it must be noted that the laser ablation itself down-cuts through the sample (ablation spot of 32 μm) and hence what was actually analyzed may largely be below the surface. In sample THA13, Mn dominates largely over Ti and is one order of magnitude higher as in samples THA16 and THA08. The Mg concentration variation seems to partly correlate with edges and fractures and can be interpreted at least in part due to equilibration with host-rock phlogopite. Along the profiles, Zn is equally present and its concentration evolution is marked by rapid variations up to one order of magnitude. In some parts of the kyanite crystals, Zn is almost as abundant as Mn, Ti and Mg. These variations are not related to any characteristic feature of the crystals. The other elements do not show any obvious correlations. V is found above the limit of detection (1 ppm) only in sample THA16. No systematic evolution of Cr could be observed, because of concentration too close to the limit of detection (15 ppm). Pb shows the same evolution as the elements attributed to alteration and post-crystallization re-equilibration, with higher concentrations at the edges of the crystals and within the fractures.

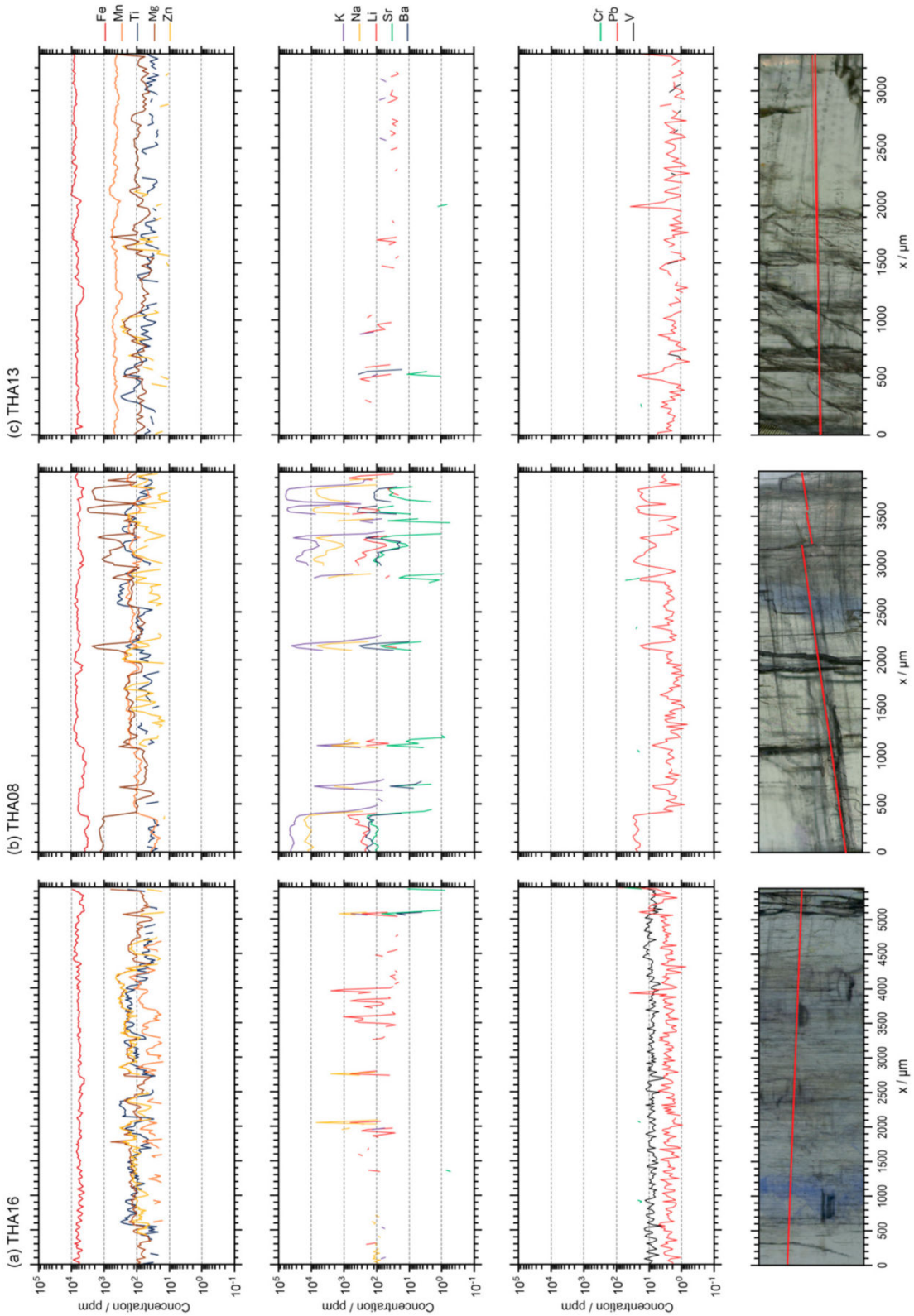

Figure 13. Quantitative Laser Ablation-Inductively Coupled Plasma Mass Spectroscopy (LA-ICPMS) analyses (in ppm) on the <100> faces of blue-green THA16 (**a**), yellow THA08 (**b**) and orange THA13 (**c**) kyanite samples from border to border of the crystals. The location of the profiles (red line) is approximately at the same position as that of EPMA analyses. The element concentration lines might be discontinuous due to values below detection limit.

4.7.6. UV-Near-Infrared Spectroscopy

All spectra (blue, yellow and orange kyanite samples) show an absorption continuum rising from infrared or mid-visible to UV, making absorption range from 315 nm to below (Figure 14). They also all show sharp and weak absorption peaks at 370, 382, 432, 446 nm. Spectra of blue samples are dominated by large absorption bands at 520 and 620 nm that, combined with the previous spectral features, generate a transmission window around 480 nm, in the blue sample. Spectra of orange and yellow kyanite samples are similar. In addition to the common spectral features described initially, both show a band at about 470 nm and a weaker band at 890 nm. These two bands are weaker in the yellow than in the orange kyanite sample. As a consequence, transmission increases from the green (550 nm) toward the infrared, hence the orange and yellow colors of the samples. The allocation of these spectral features to specific ions or defects is proposed in the Discussion section.

4.8. Phase Diagram Calculation of the Paragneiss

The *PT* pseudo-section is presented in Figure 15 for the *PT* range of ca. 550–750 °C and ca. 5.5–10.5 kbars. Calculation results show that the assemblage Grt–St–Bt–Pl–Ky–Qtz–Ti–Hem formed between 630–710 °C and 7.8–10.4 kbars, in the upper amphibolite facies. Calculations in the different systems, ranging from NCKFMASH to MnNCKFMASHT(O), allow for discussing the effects of MnO, TiO_2 and Fe_2O_3. The addition of MnO results in an expansion of the garnet stability field with the garnet-in line shifting to lower temperatures and pressures. Because of the occurrence of Ti-bearing hematite in the mica schists, the role of oxidation on phase relations was investigated through a *T*-XFe_2O_3 phase diagram section. The addition of TiO_2 and Fe_2O_3 controls the field stability of Fe^{2+}–Fe^{3+}–Ti oxide phases. The minimum XFe_2O_3 value to stabilize the Ti-bearing hematite instead of rutile is 0.1 (at constant P = 8.5 kbars). It appears that the stable assemblage garnet (Grt)–staurolite (St)–biotite (Bt) –plagioclase (Pl)–kyanite (Ky)–quartz (Qtz) with Ti–hematite (Ti–Hem) is stable between ca. 630 and 710 °C for a median XFe_2O_3 (Fe_2O_3/(Fe_2O_3 + FeO)) of 0.5 (Figure A2). In consequence the phase diagram section was computed with this XFe_2O_3 molar ratio. Considering the *P*-*T* range used for this pseudosection (550–750 °C; 5.5–10.5 kbars), hematite-rich ilmenite with ca. 50–70% of hematite end-member is stabilized in each stability field of ilmenite and, thus, labelled as "Ti–Hem" in Figure 15. For the specific *PT* field of the described paragenesis (ca. 670 °C and 9.1 kbars), the calculated ilmenite in the ilmenite–hematite solid solution is around 33%, consistent with the 10–35 % measured by EPMA (Table S6a).

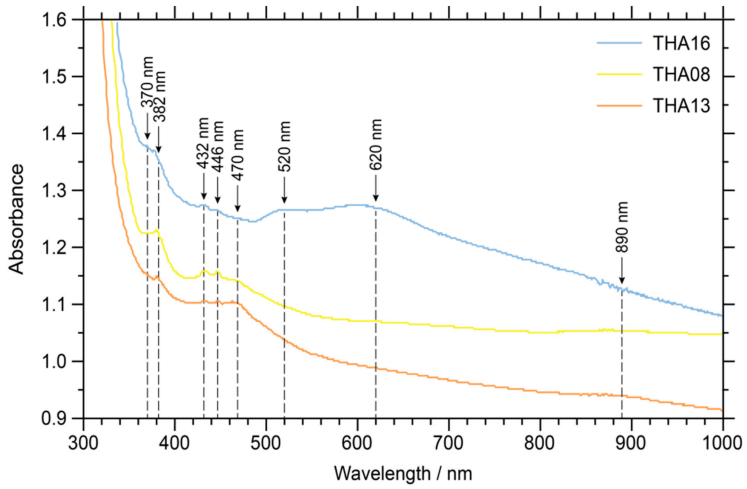

Figure 14. UV near-infrared spectra of kyanite of various colors. Spectra are shifted and re-scaled vertically for clarity. Absorbance values are those of sample THA08.

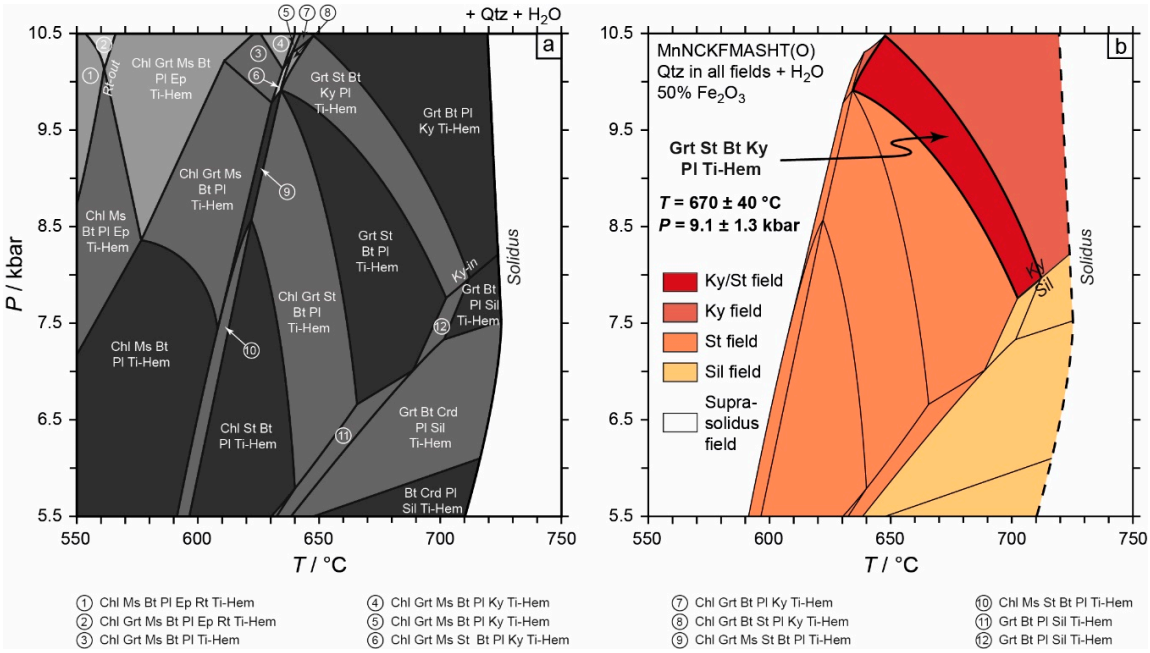

Figure 15. PT pseudo-section calculated for sample CS16_292b. (**a**) Pseudo-section showing labelled metamorphic assemblage fields. Assemblage fields are shaded according to the number of degrees of freedom, with higher-variance assemblages represented by darker shading. Ky-in and Rt-out lines are shown. (**b**) Highlight of the stability fields of kyanite, staurolite and sillimanite index minerals. The interpreted peak metamorphic assemblage field is shaded in red and labelled with bold text. Ky-Sil univariant line is shown. The right white domain corresponds to the supra-solidus field. Dashed line represents the solidus. Mineral abbreviation: biotite (Bt), chlorite (Chl), cordierite (Crd), epidote (Ep), garnet (Grt), kyanite (Ky), muscovite (Ms), plagioclase (Pl), quartz (Qtz), rutile (Rt), sillimanite (Sil), staurolite (St) and Ti-hematite (Ti-Hem).

Chlorite thermometry [70] made on retrogressed phlogopite of the paragneiss CS16_292b and schist sample KT03 indicates temperatures in the range 398–334 °C (Table S2c for phlogopite and Table S11a,b for chlorite composition). The values given by the clinochlore analyzed within sample piemontite–andalusite–muscovite–kyanite schist KT07 are in the range 280–326 °C (Table S11c), while the values from Mn-bearing clinochlore from the late brittle vein MB13 are from 233 to 315 °C (Table S11d).

5. Discussion

The Trikorfo area on Thassos Island represents a unique mineralogical locality where near gem-quality Mn-rich minerals are described. A detailed structural/mineralogical study permits to describe metamorphic parageneses and local metasomatic assemblages. The dominant formation is made of paragneisses/mica schists containing a metamorphic paragenesis, including kyanite. Towards the top of the formation, different units are described parallel to the metamorphic foliation, with some of them bearing large and colored minerals: (i) calc-silicate dominated horizons, (ii) Mn-rich schist layers and quartz lenses, (iii) kyanite-bearing quartz-feldspar coarse-grained veins, and (iv) late brittle veins cross-cutting the metamorphic foliation. The discussion is divided into three parts where (i) the near gem-quality minerals are described and the elemental substitutions leading to their color variation are discussed, (ii) the distinction between metamorphic parageneses and local metasomatic assemblages is made, (iii) a *PT*-deformation exhumation path for the conditions of formation of the different units is proposed. Kyanite is found within the metamorphic paragenesis and as near gem-quality in quartz-feldspar coarse-grained veins; it is therefore the guidance mineral of the study and the discussion.

5.1. Colored Minerals and Cation Substitution in the Trikorfo Area, Thassos Island

Dispersed metal ions in silicate and calc-silicate crystal structures lead to color variation of particular interest for mineral collectors. Silicate and calc-silicate minerals of the Trikorfo area are large and vividly colored, close to gem-quality. Moreover, thanks to trivalent cation substitutions (Mn^{3+} and Fe^{3+}) with Al, the area hosts an outstanding variety of colors within the minerals. This chapter aims to depict the main substitutions observed within kyanite, andalusite, epidote and garnet minerals.

The common natural color of kyanite (Al_2SiO_5) is blue but it can also be green, yellow, orange, white, black, grey or colorless as a function of the nature of elemental substitutions [4]. Moreover, several alternating colors can be found along bands parallel to the *c*-axis in a single kyanite crystal, marking the presence of trace elements in the crystal structure. Kyanite has two Al sites in six-coordination and one Si site in four-coordination. The occupying site and bonding state of transition elements determine the color and physical properties of the crystals [71]. In the Trikorfo area, besides syn-metamorphic crystals, kyanite (zoned blue to green/yellow-transparent, yellow and orange) is also observed in quartz-feldspar coarse-grained veins or in quartz lenses. Bulk chemical composition analyses reveal that each type of color kyanite has its own signature with a characteristic distribution of measured oxides and trace elements in the minerals (Figures 9 and 10). V and Cr distribution is markedly different between zoned blue (up to ~10 ppm and ~2 ppm, respectively) and orange kyanite (below detection limit and up to ~15 ppm, respectively), suggesting a local control from the host-rock composition. However, the low concentrations point to a similar felsic origin [4] that should be attributed to interaction with the main paragneiss unit of the area. Orange kyanite localities are very rare on Earth. The Loliondo deposit (Tanzania) is characterized by elevated MnO content up to 0.23 wt. %. Polarized optical absorption spectra show that the orange coloration is governed by crystal field d-d transitions of Mn^{3+} replacing Al in six-fold coordinated triclinic sites of the kyanite structure [9]. Even if orange kyanite from the Trikorfo area is richer in MnO than the yellow and blue zoned crystals, their MnO content (0.07 wt. % for the bulk sample analysis and locally up to 0.16 wt. % for EPMA analyses) remain far below that of orange kyanite from Tanzania. This is consistent with an orange color less intense in kyanite from Trikorfo than from Loliondo. All kyanite samples show Zn in a significant amount but without any evident correlation with crystal structure or color. The total Cr content is higher in the yellow/orange samples than in the blue kyanite (Figure 10). However, LA-ICPMS sections do not show conclusive information regarding the distribution of Cr due to concentration close to the limit of detection of 15 ppm (Figure 13). Moreover, kyanite colored by Cr^{3+} shows absorption spectra dominated by two broad absorption bands centered at 405–420 nm and 595–625 nm [72,73]. No such absorptions are observed in any of our samples, making Cr^{3+} an unrealistic chromophore in this case. This is consistent with Cr content very low in our samples (typically 1 to 20 ppm; Figure 10; Table S1c) compared to blue kyanite colored by dispersed Cr^{3+} (typically Cr_2O_3 > 1 wt. %; [73]). Hereafter, only Mn^{3+}, Fe^{3+} and Fe^{2+}–Ti^{4+} substitutions with Al^{3+} are thus discussed. The kyanite crystals analyzed by UV-near infrared spectroscopy show weak absorption bands at 370, 381, 432 and 446 nm due to isolated Fe^{3+} [7]. The large absorption bands at 520 and 620 nm, responsible for the blue color of THA16, are due to Fe^{2+}–Ti^{4+} inter-valence charge transfer (IVCT; [74–76]). No spectral features due to the Fe^{2+}-Fe^{3+} IVCT were found. In the spectra of yellow (THA08) and orange (THA13) kyanite samples, the band at 470 nm, that importantly contributes to color, is consistent with the main band attributed to isolated Mn^{3+} [9]. Hence, the origin of the yellow to orange color in our samples is attributed to isolated Mn^{3+}, with some minor contribution of isolated Fe^{3+}. The contribution of the weak 890 nm band remains unattributed.

EPMA X-ray maps and LA-ICPMS profiles show some relation between the blue zones and the Ti content of the zoned kyanite crystals THA16 and THA08 (Figure 12a,b and Figure 13a,b). Interestingly, orange kyanite (THA13) contains more TiO_2 than blue, zoned crystals. This shows that the presence of Ti alone is not sufficient to generate a blue color: Ti^{4+} atoms need to be crystallographically linked to Fe^{2+} atoms for the charge-transfer phenomenon to occur, and hence the blue color to appear. If for any reason, the charge transfer does not occur (titanium atoms may be isolated, or iron ions may be trivalent), the blue color due to IVCT does not appear. A similar behavior is documented in other

colored minerals such as corundum: some yellow sapphires sometimes contain more titanium than blue sapphires colored by Fe^{2+}–Ti^{4+} IVCT, e.g., [77]. Again, in this case, titanium concentration alone is not correlated with the blue color.

Orange kyanite is associated with green andalusite in quartz lenses (Figure 3f). Mn^{3+} might substitute for Al^{3+} in andalusite mineral formula, resulting in deep green, Mn-rich andalusite (Al, Mn)$_2$SiO$_5$ [10,78]. This andalusite variety is named viridine in reason of its brilliant green color [12]. Viridine occurrences (Germany, Belgium, Japan, Australia, Brazil and Tanzania) usually provide small or altered crystals [16,78]. Large viridine crystals of the Trikorfo area reach up to ten centimeters large, are vivid-to-deep green and unaltered. Their occurrence is promising for exploration of gem-quality, marketable viridine in the area. Compared to kyanite and sillimanite, andalusite incorporates maximum contents of Mn^{3+} due to its crystal structure [2]. Experimental works quantified that the Mn_2SiO_5 end-member cannot be higher than 6 mol% for kyanite and 1.7 mol % for sillimanite, but can reach 22 mol % for andalusite [2,79]. In the present study, Mn_2O_3 can reach up to 15.98 wt. %, yielding 17.5 mol % $Mn_2Si_2O_5$, close to the maximum possibly accepted by andalusite.

In the Trikorfo area, epidote group minerals are represented by green epidote, pink to red Mn-rich epidote and Mn-rich clinozoisite (variety clinothulite), purple piemontite, and allanite, which is only reported at the thin-section scale by Voudouris et al. [20]. Epidote, clinozoisite and piemontite represent the Fe-, Al- and Mn-rich end-members respectively of the epidote mineral family. Solid solution involves substitution of trivalent cations (Al^{3+}, Fe^{3+} or Mn^{3+}) in three non-equivalent octahedral sites in the basic formula for epidote $Ca_2M^{3+}Al_2Si_3O_{12}(OH)$ [66,67]. True piemontite (up to 12.69 wt. % Mn_2O_3) is restricted to Mn-rich andalusite bearing samples, indicating that these mica schist layers are locally particularly enriched in manganese. Mn-bearing epidote (up to 7.76 wt. % Mn_2O_3) is usually associated with spessartine-Mn oxides-quartz assemblages. The Mn-poor clinozoisite/epidote and Mn-poor clinozoisite (clinothulite) from the Trikorfo area contain up to 0.72 wt. % Mn_2O_3 which is responsible for their pink to red color. In accordance to Bonazzi and Menchetti [80] and Franz and Liebscher [67] the coloration in pink epidote/clinozoisite is due to Mn^{3+} and not Mn^{2+} in the mineral structure.

Four types of garnet are recognizable on the basis of their colors: (i) syn-metamorphic millimetric red almandine (± pyrope)-spessartine, (ii) plurimillimetric Ca–Fe-rich yellow to orange spessartine within the green horizons, (iii) centimetric almost pure pale yellowish brown grossular associated with epidote and clinozoisite in calc-silicate aggregates, and (iv) centimetric deep amber orange almost pure spessartine associated with Mn-rich andalusite, muscovite and orange kyanite. The colors of these garnet crystals directly reflect their main dominant cation (Ca^{2+}, Fe^{2+} or Mn^{2+}). Mn-rich garnet is found within the metamorphic assemblage and the composition to almost pure spessartine is only very localized to certain mica schist layers in association with orange kyanite and green andalusite, and to brittle veins cross-cutting Mn-rich horizons close to the top of the Trikorfo area.

5.2. Metamorphic Parageneses versus Metasomatic Assemblages

The Trikorfo area is dominated by garnet–kyanite–biotite–hematite–plagioclase ± staurolite ± sillimanite paragneisses/mica schists (sample CS16_292b), with intercalations of metacarbonate units near the base and top of the formation and local calc-silicate layers and Mn-rich mica schists, also close to the top of the formation. Field and mineralogical observations suggest that the epidote-grossular-bearing calc-silicate layers represent local inhomogeneities in the bedding of the sedimentary protoliths and/or compositional changes that have been produced by localized metasomatic processes during regional metamorphism, as suggested for similar layers at Therapio, Evros area [81]. In this sense, the mineralogy of the calc-silicate layers could have developed during prograde metamorphism of a Mn-rich, calcareous pelitic protolith, followed by vein formation and local metasomatic reactions during retrograde metamorphism accompanying the exhumation of Thassos Island during the Oligocene-Miocene.

Alternatively, the skarn-similar mineralogy of the calc-silicate layers (e.g., grossular, diopside, hornblende and epidote) could have been formed by fluids released by granitoids during contact

metamorphism with the carbonate (calcite and dolomite) rocks found at the top of the Trikorfo area. With the lack of radiometric data, the exact age (i.e. Hercynian?) of the orthogneiss at Trikorfo is not known but is likely older than alpine deformation. Although not exposed on Thassos Island, Oligo-Miocene magmatism is described nearby in the Rhodope area with the intrusion of syntectonic plutons 30 km to the north of Thassos Island, e.g., [52–54]. Melfos and Voudouris [27] considered that widespread gold mineralization in the area is related to this Miocene magmatic activity. Tourmaline at Trikorfo also occurs as a retrograde mineral, resulting in tourmalinite and quartz-tourmaline veins cross-cutting the metamorphic foliation. According to van Hinsberg et al. [82] metasomatic introduction of boron on the retrograde path is most commonly associated with the intrusion of late granites in orogenic belts.

The Trikorfo area shows the superposition of late secondary minerals over the metamorphic paragenesis. These silicates and calc-silcates, including a large variety of garnet and epidote composition, kyanite, andalusite, diopside, hornblende, Ti-hematite, magnetite and tourmaline indicate post-metamorphic metasomatic reactions where hot, chemically active fluids that altered the metamorphic assemblage. Furthermore Mn-rich mineralogical assemblages are found. This type of assemblage is relatively rare on Earth because it requires highly oxidized environments [15–18]. The large diversity of mineral compositions and assemblages observed at the scale of the Trikorfo area points to a local control on the mineralogy and fO_2 conditions during post-metamorphic metasomatic reactions.

For example, five different garnet-epidote assemblages are described with increasing oxidation state as indicated by the amount of Mn_2O_3 in the epidote: (i) Mn-poor grossular (up to 3.60 wt.% MnO) and Mn-poor epidote to clinozoisite (up to 1.01 wt. % Mn_2O_3) within the calc-silicate aggregates, (ii) Mn-poor spessartine (up to 24.91 wt. % MnO) associated with Mn-poor epidote (up to 1.16 wt. % Mn_2O_3) in the green horizons within gneiss host-rock, (iii) Mn-rich spessartine (up to 36.95 wt. % MnO) with Mn-rich epidote (up to 7.76 wt. % Mn_2O_3) within the spessartine–epidote–braunite–hornblende schist, (iv) almost pure spessartine (up to 42.87 wt. % MnO) associated with piemontite (up to 12.69 wt. % Mn_2O_3), Mn-rich andalusite (up to 15.98 wt. % Mn_2O_3) and orange Mn-bearing kyanite in piemontite–andalusite–muscovite–kyanite mica schists, and (v) spessartine-clinochlore-epidote (up to 6.67 wt. % Mn_2O_3). In concordance with the experimental observations of Keskinen and Liou [18], garnet which coexists with piemontite is uniformly more spessartine-rich.

Garnet and epidote are minerals showing large Fe–Al–Mn solid solutions sensitive to *PT* and fO_2 environmental conditions. In the case of epidote composition, oxygen fugacity is more important than temperature [18]. Due to extensive solid solution in terms of Mn/Fe and (Mn + Fe)/Al, Mn-rich garnet and epidote may coexist with element ratio of the different phases sensitive to temperature and degree of oxidation. With decreasing fO_2, piemontite becomes poorer in Mn and garnet and epidote minerals might tend to become more aluminous with increasing temperature [18].

Spessartine can be stable over a wide range of fO_2 and *PT* conditions from greenschist to amphibolite-granulite facies and is evidence of elevated amounts of Mn in the rock [15,83,84]. Natural occurrences of piemontite have shown evidence for metamorphism at high oxygen fugacity [18]. A highly oxidizing environment is shown by the presence of Ti-hematite, Fe^{3+}- and Mn^{3+}-rich epidote, Mn^{3+}-rich andalusite, Fe^{3+}–Mn^{3+}-rich kyanite, and so on. The intercalation of decimeter-thick layers of epidote-spessartine-Mn-rich andalusite in less oxidized levels with epidote-spessartine(almandine) assemblages implies (i) significant fO_2 gradients at restricted scale, and (ii) internally controlled fO_2 resulting from oxidized protoliths containing minerals such as Mn-oxides capable of buffering fO_2 to high pressure levels during metamorphism [17,18]. Preservation of the fO_2 gradients supports evidence for a reduced mobility of oxygen throughout high-pressure metamorphism [17] or the localized circulation of highly oxidized fluids during metasomatism. The strong variability of fO_2 dependent mineral assemblages, at all scales, within the Trikorfo area thus indicates a strong local buffering of fO_2 during post-metamorphic metasomatic reactions. As for fO_2, the mineralogical assemblages also suggest a local control in Mn concentration. Indeed, Mn-rich layers, which are mostly found at the top of the series, are scarce and never exceed a few centimeters thick.

Orange kyanite was found coexisting together with Mn-rich andalusite in quartz-feldspar coarse-grained veins and as post-deformation assemblages in mica schists towards the top of the unit in the Trikorfo area. Mn-rich andalusite may also have formed during decompression in veins within host rocks containing kyanite, e.g., [85]. However, petrographic observations suggest growth at equilibrium between kyanite and andalusite. Co-existing Al_2SiO_5 polymorphs occur in various metamorphic rocks and may form either during regional metamorphism or a combination of regional and contact metamorphism [86,87]. When kyanite, sillimanite and andalusite are free of chemical impurities, their equilibrium coexistence is invariant. However, these three polymorphs show extensive solid solution and can incorporate significant amounts of Fe^{3+} and Mn^{3+}, substituting for Al, in highly oxidized rocks [16,88,89]. This results in an increase of the variance of the system and the possible coexistence of kyanite, andalusite and sillimanite in mutual equilibrium over a measurable range of *PT* conditions [90]. The presence of Mn-bearing andalusite, and especially the association with braunite, quartz and spessartine, indicates high fO_2 [15].

Structural and mineralogical observations thus point to a two-stage evolution of the Trikorfo area, where metamorphic units were affected locally by metasomatic events during exhumation. Fluid circulation leads to fluid-rock interactions and crystallization of large, vividly-colored minerals. The chemistry of the metasomatic mineralogical assemblages is controlled by the chemistry of the protolith more or less enriched in manganese and by local fO_2 buffer.

5.3. PT-Deformation Conditions of Metamorphic Equilibrium and Metasomatic Reactions

The Rhodope domain exposes a large variety of H*P*-rocks of the Variscan continental crust and Mesozoic sediments that were subjected to Alpine subduction (Early Cretaceous-Eocene) and subsequent exhumation (Early Oligocene-Miocene) [91]. The recorded conditions can be as high as >19 kbars and 750–800 °C with local partially amphibolitized kyanite eclogites, e.g., [37,91].

Thassos Island, belonging to the South Rhodope metamorphic core complex, displays Oligocene to Miocene metamorphic and exhumation history [36,40]. In response to crustal thickening during Alpine tectonics, the geothermobarometric analyses of amphibole gneisses suggest metamorphic conditions of approximately 620 °C/4.7 kbars for the lower unit and 580 °C/2.4 kbars for the intermediate unit [47,48]. On the basis of the observation of a garnet–kyanite–sillimanite assemblage, Dimitriadis [24] estimated the conditions achieved by the mica schists of the Trikorfo area around 5.5 ± 1.5 kbars and 600 ± 50 °C. Brun and Sokoutis [40] reported an unreferenced personal communication of Kostopoulos (2004) stating that the garnet amphibolites yielded temperatures ranging from 545 to 660 °C, as described in Dimitriadis [24], but at significantly higher pressures from 6.5 to 9.5 kbars. On the basis of the garnet–staurolite–kyanite–plagioclase–quartz–phlogopite–Ti–hematite assemblage, our thermodynamic modeling indicates metamorphic conditions at Trikorfo of ca. 9.1 ± 1.3 kbars and 670 ± 40 °C, at significantly higher *P* and *T* conditions than previously estimated. The field given in Figure 15 is the only one where kyanite and staurolite are stable together. Instead of staurolite, Dimitriadis [24] reported the presence of sillimanite growing at the expense of kyanite within the metamorphic gneiss. The conditions of the Trikorfo formation should rather stand in the high-temperature/low-pressure part of the domain indicated by our stable metamorphic assemblage, with sillimanite post-dating kyanite. The MnO content of the calculated equilibrated garnet composition is a bit higher than that measured in sample CS16_292b. It is probably due to the fact that the solid solution model used in our thermodynamic calculation is not fully appropriate. The addition of MnO in the system has a small effect on the garnet mode but a great effect on the garnet stability field. Indeed, in agreement with White et al. [92], the incorporation of MnO in our phase diagram calculations (in the MnNCKFMASHT(O) system) leads to a shift to lower *PT* conditions of the garnet-in line, compared to a system without MnO. The *PT* conditions obtained for the peak metamorphic assemblage recorded by the kyanite-bearing paragneisses are in good agreement with the geological context and therefore we are confident with the calculated phase diagram, even if the modeled garnet composition is not strictly the same than the measured one. Indeed, this M*P*-H*T* metamorphism recorded by paragneisses

from the intermediate unit is comparable to those estimated at the Thassos scale. This amphibolite metamorphism, which is associated with the continuous development of the extensive low-angle S_n foliation since ductile to brittle deformation, could mark the beginning of the nappe stack exhumation.

Kyanite and kyanite–andalusite assemblages are found at the interface between metamorphic host rock and quartzo–feldspathic veins. The crystals are generally weakly deformed and aligned parallel to regional lineation. This indicates a local reaction where a SiO_2-rich fluid interacts with the Al_2O_3-rich host-rock [93], as indicated by their Cr/V ratio [4], to form either kyanite or kyanite-andalusite as a function of the *PT* conditions and the variance of the system linked to available MnO [90]. This reaction occurs at ductile conditions while the rock still records stretching lineation. The temperatures derived from the Ti-in kyanite thermometer from Müller et al. [4] are in the range 670–790 °C coherent with the Perple_X modeling. This would then indicate that metasomatic kyanite form at or close to the metamorphic peak conditions. However, EPMA and LA-ICPMS data (Figures 12 and 13) show that Ti distribution is variable within the crystals and these temperatures should be considered with caution. Except for some of the kyanite and andalusite crystals, the other metasomatic silicate and calc-silicate minerals of Thassos are usually not oriented. Dimitriadis [24] suggested retrogression under static conditions as evidenced by undeformed matted fibrolite and unoriented growth of chlorite. However, continuous deformation during the main kinematic event is evidenced by coherent stretching and mineral lineation and brittle vein opening to temperatures as low as 230 °C, as indicated by clinochlore growth in late brittle veins. The presence of non-oriented minerals should be the result of crystal growth from hydrothermal fluids during metasomatic reactions. The presence of calc-silicate minerals (grossular, diopside, hornblende, epidote), especially located to the top of the series where the paragneisses/mica schists are in contact with marble units, implies decarbonation during metasomatic reactions.

6. Conclusions

The garnet–kyanite–biotite–hematite–plagioclase ± staurolite ± sillimanite paragneiss of the Trikorfo area (Thassos Island, Rhodope Massif, northern Greece) recorded metamorphic conditions of ca. 670 ± 40 °C and ca. 9.1 ± 1.3 kbars. Structural, petrographic and mineralogical observations indicate that localized metasomatic reactions occurred during the exhumation of the H*P* unit locally containing layers enriched in Mn with a strong local fO_2 buffering. Metasomatism is likely the result of Miocene intrusion of granitoids, which are related to ore deposits on Thassos Island. Metasomatic reactions first occurred under ductile conditions in an extensive context close to the kyanite-andalusite stability curve and continued until purely brittle conditions as indicated by the presence of late veins cross-cutting the metamorphic foliation. The result is a mineralogical site that could be regarded as a unique geotope with uncommon (Mn-rich) silicate and calc-silicate mineral assemblages similar to what is observed in skarn deposits where hot active hydrothermal fluids interact with carbonate rocks.

Crystals of kyanite, green andalusite, garnet (grossular and spessartine) and red epidote–clinozoisite are large (up to several centimeters), show vivid colors, and are suitable for cabochon-shaped gemstones. As such, the Trikorfo locality can be regarded as a promising area for the exploration of true, facetable gemstones. Their genesis due to metasomatic reactions also underlines the important role of metasomatism for gemstone formation in general, as previously noted in the literature [94–96].

Our combined petrographic, geochemical and spectroscopic observations permit us to demonstrate that the orange color of kyanite in the Trikorfo area is mainly due to Mn^{3+} substitution. Although the Mn content is significantly lower than that in the Loliondo (Tanzania) deposit, Thassos Island (Rhodope, Greece) can now be classified as the second locality worldwide where Mn-rich orange kyanite is reported.

Supplementary Materials: The following are available online at http://www.mdpi.com/2075-163X/9/4/252/s1, Table S1: Bulk rock analyses, Table S2: EPMA analyses PHLOGOPITE, Table S3: EPMA analyses PLAGIOCLASE, Table S4: EPMA analyses GARNET, Table S5: EPMA analyses STAUROLITE, Table S6: EPMA analyses Ti-HEMATITE, Table S7: EPMA analyses EPIDOTE, Table S8: EPMA analyses DIOPSIDE-HORNBLENDE,

Table S9: EPMA analyses TITANITE-RUTILE, Table S10: EPMA analyses MnOXIDES, Table S11: EPMA analyses CHLORITE, Table S12: EPMA analyses KYANITE, Table S13: EPMA analyses ANDALUSITE.

Author Contributions: Conceptualization, A.T.; Data curation, A.T.; Funding acquisition, A.T. and P.V.; Investigation, A.T., P.V., A.E., C.S., K.T., M.B., B.R., C.M., I.G., M.E. and C.P.; Software, A.E.; Writing—original draft, A.T. and P.V.

Funding: This research was partly funded by LABEX ANR-10-LABX-21-Ressources21, Nancy, France, TelluS Program of CNRS/INSU, and OTELo (Observatoire Terre et Environnement de Lorraine, Université de Lorraine, France).

Acknowledgments: The authors warmly acknowledge A. Flammang, J. Moine and O. Rouer (GeoRessources lab., Univ. Lorraine, France) and P. Stutz and S. Heidrich (Institute of Mineralogy and Petrology, University of Hamburg, Germany) for the quality of sample preparation and EPMA analyses. We are grateful to R. Mosser-Ruck (GeoRessources lab., Univ. Lorraine, France) for fruitful discussions. Three anonymous journal reviewers are thanked for their helpful and constructive comments.

Conflicts of Interest: The authors declare no conflict of interest.

Appendix A

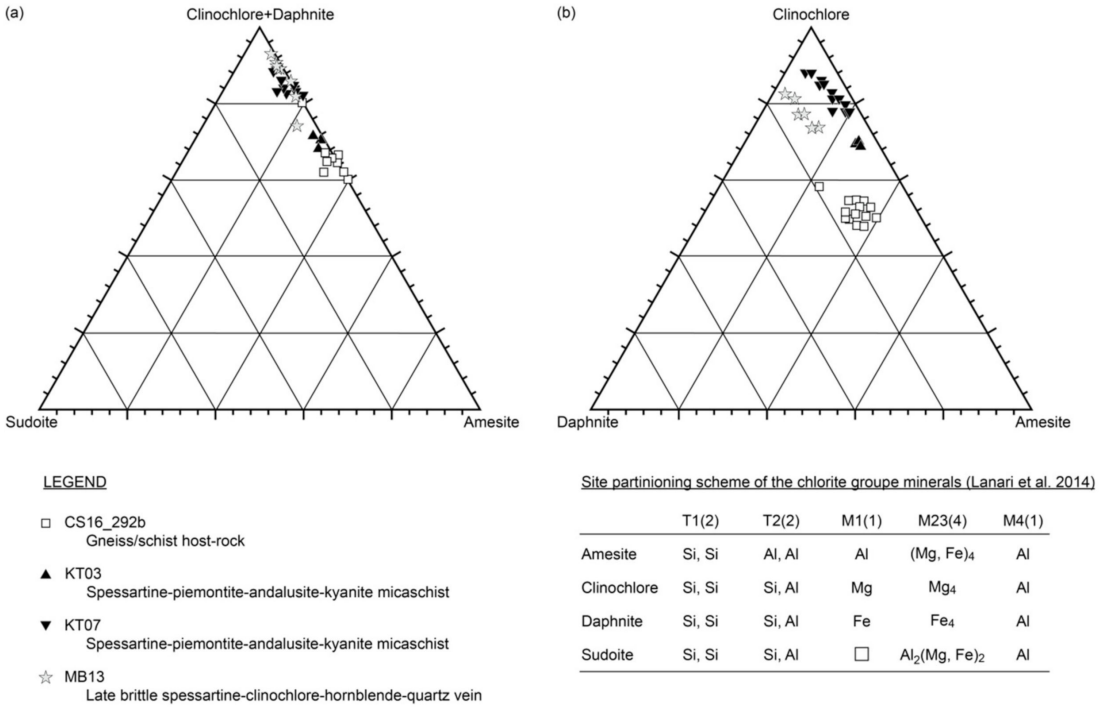

Site partinioning scheme of the chlorite groupe minerals (Lanari et al. 2014)

	T1(2)	T2(2)	M1(1)	M23(4)	M4(1)
Amesite	Si, Si	Al, Al	Al	$(Mg, Fe)_4$	Al
Clinochlore	Si, Si	Si, Al	Mg	Mg_4	Al
Daphnite	Si, Si	Si, Al	Fe	Fe_4	Al
Sudoite	Si, Si	Si, Al	□	$Al_2(Mg, Fe)_2$	Al

Figure A1. Composition of chlorite-group minerals analyzed by EPMA in (**a**) Clinochlore + Daphnite–Sudoite–Amesite and (**b**) Clinochlore–Daphnite–Amesite ternary plots. The mineral names are according the site partitioning scheme used in Lanari et al. [97].

Appendix B

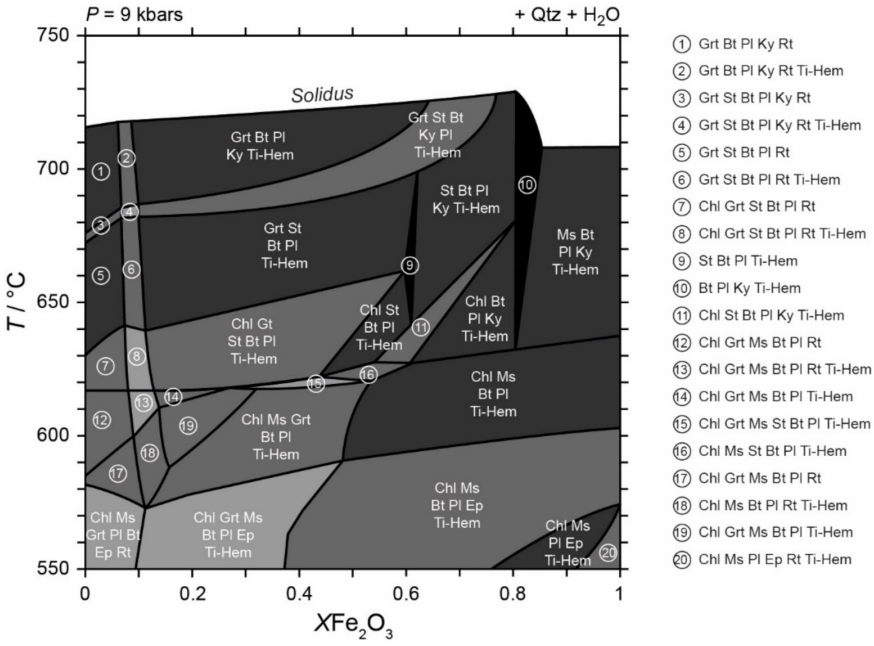

Figure A2. T-XFe_2O_3 pseudosection calculated for 9 kbars and 550–750 °C for sample CS16_292b. Assemblage fields are shaded according to the number of degrees of freedom, with higher-variance assemblages represented by darker shading. Mineral abbreviation: biotite (Bt), chlorite (Chl), epidote (Ep), garnet (Grt), kyanite (Ky), muscovite (Ms), plagioclase (Pl), quartz (Qtz), rutile (Rt), staurolite (St) and Ti-hematite (Ti-Hem).

References

1. Abs-Wurmbach, I.; Langer, K. Synthetic Mn^{3+}-kyanite and viridine, $(Al_{2-x}Mn_x^{3+})SiO_5$, in the system Al_2O_3-MnO-MnO_2-SiO_2. *Contrib. Mineral. Petrol.* **1975**, *49*, 21–38. [CrossRef]
2. Abs-Wurmbach, I.; Langer, K.; Seifert, F.; Tillmanns, E. The crystal chemistry of (Mn^{3+}, Fe^{3+})-substituted andalusites (viridines and kanonaite), $(Al_{1-x-y}Mn_x^{3+}Fe_y^{3+})_2(O|SiO_4)$: Crystal structure refinements, Mössbauer, and polarized optical absorption spectra. *Z. Für Krist.* **1981**, *155*, 81–113.
3. Pearson, G.R.; Shaw, D.M. Trace elements in kyanite, sillimanite and andalusite. *Am. Mineral.* **1960**, *45*, 808–817.
4. Müller, A.; van den Kerkhof, A.M.; Selbekk, R.S.; Broekmans, M.A.T.M. Trace element composition and cathodoluminescence of kyanite and its petrogenetic implications. *Contrib. Mineral. Petrol.* **2016**, *171*, 70. [CrossRef]
5. Faye, G.H.; Nickel, E.H. On the origin of colour and pleochroism of kyanite. *Can. Mineral.* **1969**, *10*, 35–46.
6. Meinhold, K.D.; Frisch, T. Manganese-silicate-bearing metamorphic rocks from central Tanzania. *Schweiz. Mineral. Petrogr. Mitt.* **1970**, *50*, 493–507.
7. Chadwick, K.M.; Rossman, G.R. Orange kyanite from Tanzania. *Gems Gemol.* **2009**, *45*, 146–147.
8. Gaft, M.; Nagli, L.; Panczer, G.; Rossman, G.R.; Reisfeld, R. Laser-induced time-resolved luminescence of orange kyanite Al_2SiO_5. *Opt. Mater.* **2011**, *33*, 1476–1480. [CrossRef]
9. Wildner, M.; Beran, A.; Koller, F. Spectroscopic characterisation and crystal field calculations of varicoloured kyanites from Loliondo, Tanzania. *Mineral. Petrol.* **2013**, *107*, 289–310. [CrossRef]
10. Hålenius, U. A spectroscopic investigation of manganian andalusite. *Can. Mineral.* **1978**, *16*, 567–575.
11. Smith, G.; Hålenius, U.; Langer, K. Low temperature spectral studies of Mn^{3+}-bearing andalusite and epidote type minerals in the range 30,000–5000 cm^{-1}. *Phys. Chem. Miner.* **1982**, *8*, 136–142. [CrossRef]
12. Klemm, G. Uber Viridin, eine Abart des Andalusites. *Not. Ver Erdk Darmstadt* **1911**, *32*, 4–13.
13. Burns Roger, G. *Mineralogical Applications of Crystal Field Theory*, 2nd ed.; Cambridge University Press: Cambridge, UK, 1970; ISBN 0-521-43077-1.

14. Manning, P.G. The optical absorption spectra of the garnets almandine-pyrope, pyrope and spessartine and some structural interpretations of mineralogical significance. *Can. Mineral.* **1967**, *9*, 237–251.
15. Abs-Wurmbach, I.; Peters, T. The Mn-Al-Si-O system: An experimental study of phase relations applied to parageneses in manganese-rich ores and rocks. *Eur. J. Mineral.* **1999**, *11*, 45–68. [CrossRef]
16. Jöns, N.; Schenk, V. Petrology of whiteschists and associated rocks at Mautia Hill (Tanzania): Fluid infiltration during high-grade metamorphism. *J. Petrol.* **2004**, *45*, 1959–1981. [CrossRef]
17. Reinecke, T. Phase relationships of sursassite and other Mn-silicates in highly oxidized low-grade, high-pressure metamorphic rocks from Evvia and Andros islands, Greece. *Contrib. Mineral. Petrol.* **1986**, *94*, 110–126. [CrossRef]
18. Keskinen, M.; Liou, J.G. Stability relations of Mn–Fe–Al piemontite. *J. Metamorph. Geol.* **1987**, *5*, 495–507. [CrossRef]
19. Voudouris, P.; Graham, I.; Melfos, V.; Sutherland, L.; Zaw, K. Gemstones in Greece: Mineralogy and Crystallizing Environment. In Proceedings of the 34th IGC Conference, Brisbane, Australia, 5–10 August 2012.
20. Voudouris, P.; Graham, I.; Mavrogonatos, K.; Su, S.; Papavasiliou, K.; Farmaki, M.-V.; Panagiotidis, P. Mn-andalusite, spessartine, Mn-grossular, piemontite and Mn-zoisite/clinozoisite from Trikorfo, Thassos island, Greece. *Bull. Geol. Soc. Greece* **2016**, *50*, 2068–2078. [CrossRef]
21. Klemme, S.; Berndt, J.; Mavrogonatos, C.; Flemetakis, S.; Baziotis, I.; Voudouris, P.; Xydous, S. On the color and genesis of prase (green quartz) and Amethyst from the island of Serifos, Cyclades, Greece. *Minerals* **2018**, *8*, 487. [CrossRef]
22. Ottens, B.; Voudouris, P. *Griechenland: Mineralien, Fundorte, Lagerstätten*; Christian Weise Verlag: München, Germany, 2018.
23. Voudouris, P.; Melfos, V.; Mavrogonatos, C.; Tarantola, A.; Götze, J.; Alfieris, D.; Maneta, V.; Psimis, I. Amethyst Occurrences in Tertiary Volcanic Rocks of Greece: Mineralogical, Fluid Inclusion and Oxygen Isotope Constraints on Their Genesis. *Minerals* **2018**, *8*, 324. [CrossRef]
24. Dimitriadis, E. Sillimanite grade metamorphism in Thasos island, Rhodope massif, Greece and its regional significance. *Geol. Rhodopica* **1989**, *1*, 190–201.
25. Voudouris, P.; Constantinidou, S.; Kati, M.; Mavrogonatos, C.; Kanellopoulos, C.; Volioti, E. Genesis of alpinotype fissure minerals from Thasos island, Northern Greece—Mineralogy, mineral chemistry and crystallizing environment. *Bull. Geol. Soc. Greece* **2013**, *47*, 468–476. [CrossRef]
26. Vason, M.; Martin, S. Metamorphosed iron-manganese deposits from the island of Thassos (Western Rhodope region, northern Greece). *Ofioliti* **1993**, *18*, 181–186.
27. Melfos, V.; Voudouris, P. Fluid evolution in Tertiary magmatic-hydrothermal ore systems at the Rhodope metallogenic province, NE Greece. A review. *Geol. Croat.* **2016**, *69*, 157–167. [CrossRef]
28. Zachos, S. Geological Map of Greece, Thassos Sheet. 1982. Available online: https://www.worldcat.org/title/geological-map-of-greece-thassos-sheet-phyllo-thasos-institogto-geologikon-kai-metalletikoi-ereunon-i-geologiki-chartografioi-egiye-apo-to-s-zachos/oclc/492645828 (accessed on 24 April 2019).
29. Su, S.; Graham, I.; Voudouris, P.; Mavrogonatos, K.; Farmaki, M.V.; Panagiotidis, P. *Viridine, Piemontite and Epidote Group Minerals from Thassos Island, Northern Greece*; AGI: Alexandria, VA, USA, 2016; T37.P2; p. 1715.
30. Voudouris, P. Minerals of Eastern Macedonia and Western Thrace: Geological framework and environment of formation. *Bull. Geol. Soc. Greece* **2005**, *37*, 62–77.
31. Voudouris, P.; Melfos, V.; Katerinopoulos, A. Precious stones in Greece: Mineralogy and geological environment of formation. In Proceedings of the Understanding the Genesis of Ore Deposits to Meet the Demand of the 21st Century, Moscow, Russia, 21–24 August 2006; p. 6.
32. Le Pichon, X.; Bergerat, F.; Roulet, M.J. Plate kinematics and tectonics leading to the Alpine belt formation: A new analysis. In *Processes in Continental Lithospheric Deformation*; Clark, S.P., Burchfiel, B.C., Suppe, J., Eds.; Geological Society of America: Boulder, CO, USA, 1988; Volume 218, pp. 111–131.
33. Dewey, J.F.; Helman, M.L.; Knott, S.D.; Turco, E.; Hutton, D.H.W. Kinematics of the western Mediterranean. *Geol. Soc. Lond. Spec. Publ.* **1989**, *45*, 265–283. [CrossRef]
34. Bonneau, M. La Tectonique de L'arc égéen Externe et du Domaine Cycladique. Ph.D. Thesis, Université Pierre et Marie Curie, Paris, France, 1991; p. 443.
35. van Hinsbergen, D.J.J.; Hafkenscheid, E.; Spakman, W.; Meulenkamp, J.E.; Wortel, R. Nappe stacking resulting from subduction of oceanic and continental lithosphere below Greece. *Geology* **2005**, *33*, 325–328. [CrossRef]

36. Wawrzenitz, N.; Krohe, A. Exhumation and doming of the Thasos metamorphic core complex (S Rhodope, Greece): Structural and geochronological constraints. *Tectonophysics* **1998**, *285*, 301–332. [CrossRef]
37. Liati, A.; Seidel, E. Metamorphic evolution and geochemistry of kyanite eclogites in central Rhodope, northern Greece. *Contrib. Mineral. Petrol.* **1996**, *123*, 293–307. [CrossRef]
38. Liati, A.; Gebauer, D. Constraining the prograde and retrograde P-T-t path of Eocene HP rocks by SHRIMP dating of different zircon domains: Inferred rates of heating, burial, cooling and exhumation for central Rhodope, northern Greece. *Contrib. Mineral. Petrol.* **1999**, *135*, 340–354. [CrossRef]
39. Liati, A. Identification of repeated Alpine (ultra) high-pressure metamorphic events by U–Pb SHRIMP geochronology and REE geochemistry of zircon: The Rhodope zone of Northern Greece. *Contrib. Mineral. Petrol.* **2005**, *150*, 608–630. [CrossRef]
40. Brun, J.-P.; Sokoutis, D. Kinematics of the Southern Rhodope Core Complex (North Greece). *Int. J. Earth Sci.* **2007**, *96*, 1079–1099. [CrossRef]
41. Moulas, E.; Kostopoulos, D.; Connolly, J.A.D.; Burg, J.-P. P-T estimates and timing of the sapphirine-bearing metamorphic overprint in kyanite eclogites from Central Rhodope, northern Greece. *Petrology* **2013**, *21*, 507–521. [CrossRef]
42. Dürr, S.; Altherr, R.; Keller, J.; Okrusch, M.; Seidel, E. The Median Aegean Crystal-line Belt: Stratigraphy, Structure, Metamorphism, Magmatism. *IUCG Sci. Rep.* **1978**, *38*, 455–477.
43. Jacobshagen, V.; Dürr, S.; Kockel, F.; Kopp, K.O.; Kowalczyk, G.; Berckhemer, H. Structure and Geodynamic Evolution of the Aegean Region. In *Alps, Apennines, Hellenides*; Cloos, H., Roeder, D., Schmidt, K., Eds.; IUCG: Stuttgart, Germany, 1978; pp. 537–564.
44. Lister, G.S.; Banga, G.; Feenstra, A. Metamorphic core complexes of Cordilleran type in the Cyclades, Aegean Sea, Greece. *Geology* **1984**, *12*, 221–225. [CrossRef]
45. Melfos, V.; Voudouris, P. Cenozoic metallogeny of Greece and potential for precious, critical and rare metals exploration. *Ore Geol. Rev.* **2017**, *89*, 1030–1057. [CrossRef]
46. Liati, A.; Fanning, C.M. Eclogites and Country rock orthogneisses representing upper Permian Gabbros in Hercynian Granitoids, Rhodope, Greece: Geochronological Constraints. *Mitt. Österr. Mineral. Ges.* **2005**, *150*, 88.
47. Schulz, B. Syntectonic heating and loading-deduced from microstructures and mineral chemistry in micaschists and amphibolites of the Pangeon complex (Thassos island, Northern Greece). *Neues Jahrb. Für Geol. Paläontol. Abh.* **1992**, *184*, 181–201.
48. Bestmann, M.; Kunze, K.; Matthews, A. Evolution of a calcite marble shear zone complex on Thassos Island, Greece: Microstructural and textural fabrics and their kinematic significance. *J. Struct. Geol.* **2000**, *22*, 1789–1807. [CrossRef]
49. Dinter, D.A. Late Cenozoic extension of the Alpine collisional orogen, northeastern Greece: Origin of the north Aegean basin. *Gsa Bull.* **1998**, *110*, 1208–1230. [CrossRef]
50. Kounov, A.; Wüthrich, E.; Seward, D.; Burg, J.-P.; Stockli, D. Low-temperature constraints on the Cenozoic thermal evolution of the Southern Rhodope Core Complex (Northern Greece). *Int. J. Earth Sci.* **2015**, *104*, 1337–1352. [CrossRef]
51. Peterek, A.; Polte, M.; Wölfl, C.; Bestmann, M.; Lemtis, O. Zur jungtertiären geologischen Entwicklung im SW der Insel Thassos (S-Rhodope, Nordgriechenland). *Erlanger Geol. Abh.* **1994**, *124*, 29–59.
52. Dinter, D.A.; Royden, L. Late Cenozoic extension in northeastern Greece: Strymon Valley detachment system and Rhodope metamorphic core complex. *Geology* **1993**, *21*, 45–48. [CrossRef]
53. Sokoutis, D.; Brun, J.P.; Driessche, J.V.D.; Pavlides, S. A major Oligo-Miocene detachment in southern Rhodope controlling north Aegean extension. *J. Geol. Soc.* **1993**, *150*, 243–246. [CrossRef]
54. Kilias, A.A.; Mountrakis, D.M. Tertiary extension of the Rhodope massif associated with granite emplacement (Northern Greece). *Acta Vulcanol.* **1998**, *10*, 331–337.
55. Carignan, J.; Hild, P.; Mevelle, G.; Morel, J.; Yeghicheyan, D. Routine Analyses of Trace Elements in Geological Samples using Flow Injection and Low Pressure On-Line Liquid Chromatography Coupled to ICP-MS: A Study of Geochemical Reference Materials BR, DR-N, UB-N, AN-G and GH. *Geostand. Newsl.* **2001**, *25*, 187–198. [CrossRef]
56. Pouchou, J.-L.; Pichoir, F. *Quantitative Analysis of Homogeneous or Stratified Microvolumes Applying the Model "PAP." In Electron Probe Quantitation*; Heinrich, K.F.J., Newbury, D.E., Eds.; Springer US: Boston, MA, USA, 1991; pp. 31–75. ISBN 978-1-4899-2617-3.

57. Jochum, K.P.; Weis, U.; Stoll, B.; Kuzmin, D.; Yang, Q.; Raczek, I.; Jacob, D.E.; Stracke, A.; Birbaum, K.; Frick, D.A.; et al. Determination of Reference Values for NIST SRM 610–617 Glasses Following ISO Guidelines. *Geostand. Geoanalytical Res.* **2011**, *35*, 397–429. [CrossRef]
58. Paton, C.; Hellstrom, J.; Paul, B.; Woodhead, J.; Hergt, J. Iolite: Freeware for the visualisation and processing of mass spectrometric data. *J. Anal. At. Spectrom.* **2011**, *26*, 2508–2518. [CrossRef]
59. Connolly, J.A.D. Computation of phase equilibria by linear programming: A tool for geodynamic modeling and its application to subduction zone decarbonation. *Earth Planet. Sci. Lett.* **2005**, *236*, 524–541. [CrossRef]
60. Holland, T.J.B.; Powell, R. An improved and extended internally consistent thermodynamic dataset for phases of petrological interest, involving a new equation of state for solids. *J. Metamorph. Geol.* **2011**, *29*, 333–383. [CrossRef]
61. White, R.W.; Powell, R.; Holland, T.J.B.; Worley, B.A. The effect of TiO_2 and Fe_2O_3 on metapelitic assemblages at greenschist and amphibolite facies conditions: Mineral equilibria calculations in the system K_2O–FeO–MgO–Al_2O_3–SiO_2–H_2O–TiO_2–Fe_2O_3. *J. Metamorph. Geol.* **2000**, *18*, 497–511. [CrossRef]
62. White, R.W.; Powell, R.; Holland, T.J.B.; Johnson, T.E.; Green, E.C.R. New mineral activity–composition relations for thermodynamic calculations in metapelitic systems. *J. Metamorph. Geol.* **2014**, *32*, 261–286. [CrossRef]
63. Newton, R.C.; Charlu, T.V.; Kleppa, O.J. Thermochemistry of the high structural state plagioclases. *Geochim. Cosmochim. Acta* **1980**, *44*, 933–941. [CrossRef]
64. Bocchio, R.; Diella, V.; Adamo, I.; Marinoni, N. Mineralogical characterization of the gem-variety pink clinozoisite from Val Malenco, Central Alps, Italy. *Rend. Lincei* **2017**, *28*, 549–557. [CrossRef]
65. Geller, S. Crystal chemistry of garnets. *Z. Krist.* **1967**, *125*, 1–45. [CrossRef]
66. Armbruster, T.; Bonazzi, P.; Akasaka, M.; Bermanec, V.; Chopin, C.; Gieré, R.; Heuss-Assbichler, S.; Liebscher, A.; Menchetti, S.; Pan, Y.; et al. Recommended nomenclature of epidote-group minerals. *Eur. J. Mineral.* **2006**, *18*, 551–567. [CrossRef]
67. Franz, G.; Liebscher, A. Physical and Chemical Properties of the Epidote Minerals: An introduction. *Rev. Mineral. Geochem.* **2004**, *56*, 1–81. [CrossRef]
68. Schreyer, W.; Bernhardt, H.-J.; Fransolet, A.-M.; Armbruster, T. End-member ferrian kanonaite: An andalusite phase with one Al fully replaced by $(Mn, Fe)^{3+}$ in a quartz vein from the Ardennes mountains, Belgium, and its origin. *Contrib. Mineral. Petrol.* **2004**, *147*, 276–287. [CrossRef]
69. Sun, S.S.; McDonough, W.F. Chemical and isotopic systematics of oceanic basalts: Implications for mantle composition and processes. *Geol. Soc. Lond. Spec. Publ.* **1989**, *42*, 313–345. [CrossRef]
70. Cathelineau, M. Cation site occupancy in chlorites and illites as a function of temperature. *Clay Miner.* **1988**, *23*, 471–485. [CrossRef]
71. Furukawa, Y.; Yoshiasa, A.; Arima, H.; Okube, M.; Murai, K.; Nishiyama, T. Local Structure of Transition Elements (V, Cr, Mn, Fe and Zn) in Al_2SiO_5 Polymorphs. *Aip Conf. Proc.* **2007**, *882*, 235–237.
72. Rossman, G.R. Optical spectroscopy. In *Spectroscopic Methods in Mineralogy and Geology*; Hawthorne, F.C., Ed.; De Gruyter: Vienna, Austria, 1988; Volume 18, pp. 205–254.
73. Platonov, A.N.; Tarashchan, A.N.; Langer, K.; Andrut, M.; Partzsch, G.; Matsyuk, S.S. Electronic absorption and luminescence spectroscopic studies of kyanite single crystals: Differentiation between excitation of FeTi charge transfer and Cr^{3+} dd transitions. *Phys. Chem. Miner.* **1998**, *25*, 203–212. [CrossRef]
74. White, E.W.; White, W.B. Electron Microprobe and Optical Absorption Study of Colored Kyanites. *Science* **1967**, *158*, 915–917. [CrossRef] [PubMed]
75. Rost, F.; Simon, E. Zur Geochemie und Färbung des Cyanits. *Neues Jahrb. Mineral.-Mon.* **1972**, *9*, 383–395.
76. Parkin, K.M.; Loeffler, B.M.; Burns, R.G. Mössbauer spectra of kyanite, aquamarine, and cordierite showing intervalence charge transfer. *Phys. Chem. Miner.* **1977**, *1*, 301–311. [CrossRef]
77. Bonizzoni, L.; Galli, A.; Spinolo, G.; Palanza, V. EDXRF quantitative analysis of chromophore chemical elements in corundum samples. *Anal. Bioanal. Chem.* **2009**, *395*, 2021–2027. [CrossRef]
78. Novák, M.; Škoda, R. Mn^{3+}-rich andalusite to kanonaite and their breakdown products from metamanganolite at Kojetice near Třebíč, the Moldanubian Zone, Czech Republic. *J. Geosci.* **2007**, *52*, 161–167. [CrossRef]
79. Abs-Wurmbach, I.; Langer, K.; Schreyer, W. The Influence of Mn^{3+} on the Stability Relations of the Al2Si05 Polymorphs with Special Emphasis on Manganian Andalusites (Viridines), $(Al_{1-x}Mn_x^{3+})_2(O/SiO_4)$: An Experimental Investigation. *J. Petrol.* **1983**, *24*, 48–75. [CrossRef]

80. Bonazzi, P.; Menchetti, S. Manganese in Monoclinic Members of the Epidote Group: Piemontite and Related Minerals | Reviews in Mineralogy and Geochemistry. *Rev. Min. Geochem.* **2004**, *56*, 495–551. [CrossRef]
81. Kassoli-Fournaraki, A.; Michailidis, K. Chemical composition of tourmaline in quartz veins from Nea Roda and Thasos areas in Macedonia, northern Greece. *Can. Mineral.* **1994**, *32*, 607–615.
82. van Hinsberg, V.J.; Henry, D.J.; Dutrow, B.L. Tourmaline as a Petrologic Forensic Mineral: A Unique Recorder of Its Geologic Past. *Elements* **2011**, *7*, 327–332. [CrossRef]
83. Symmes, G.H.; Ferry, J.M. The effect of whole-rock MnO content on the stability of garnet in pelitic schists during metamorphism. *J. Metamorph. Geol.* **1992**, *10*, 221–237. [CrossRef]
84. Geiger, C.A.; Armbruster, T. $Mn_3Al_2Si_3O_{12}$ spessartine and $Ca_3Al_2Si_3O_{12}$ grossular garnet: Structural dynamic and thermodynamic properties. *Am. Mineral.* **1997**, *82*, 740–747. [CrossRef]
85. Kerrick, D.M. *The Al_2SiO_5 Polymorphs*; Reviews in Mineralogy; Mineralogical Society of America: Washington, DC, USA, 1990; ISBN 978-0-939950-27-0.
86. Larson, T.E.; Sharp, Z.D. Stable isotope constraints on the Al_2SiO_5 'triple-point' rocks from the Proterozoic Priest pluton contact aureole, New Mexico, USA. *J. Metamorph. Geol.* **2003**, *21*, 785–798. [CrossRef]
87. Sepahi, A.A.; Whitney, D.L.; Baharifar, A.A. Petrogenesis of andalusite–kyanite–sillimanite veins and host rocks, Sanandaj-Sirjan metamorphic belt, Hamadan, Iran. *J. Metamorph. Geol.* **2004**, *22*, 119–134. [CrossRef]
88. Abraham, K.; Schreyer, W. Minerals of the viridine hornfels from Darmstadt, Germany. *Contrib. Mineral. Petrol.* **1975**, *49*, 1–20. [CrossRef]
89. Kramm, U. Kanonaite-rich viridines from the Venn-Stavelot Massif, Belgian Ardennes. *Contrib. Mineral. Petrol.* **1979**, *69*, 387–395. [CrossRef]
90. Grambling, J.A.; Williams, M.L. The Effects of Fe^{3+} and Mn^{3+} on Aluminum Silicate Phase Relations in North-Central New Mexico, U.S.A. *J. Petrol.* **1985**, *26*, 324–354. [CrossRef]
91. Mposkos, E.; Krohe, A. Petrological and structural evolution of continental high pressure (HP) metamorphic rocks in the Alpine Rhodope Domain (N. Greece). In *Proceedings, Third International Conference on the Geology of the Eastern Mediterranean*; Panayides, I., Xenophontos, C., Malpas, J., Eds.; Geological Survey Department: Nicosia, Cyprus, 2000; pp. 221–232.
92. White, R.W.; Powell, R.; Johnson, T.E. The effect of Mn on mineral stability in metapelites revisited: New a–x relations for manganese-bearing minerals. *J. Metamorph. Geol.* **2014**, *32*, 809–828. [CrossRef]
93. El Mahi, B.; Zahraoui, M.; Hoepffner, C.; Boushaba, A.; Meunier, A.; Beaufort, D. Kyanite-quartz synmetamorphic veins: Indicators of post-orogenic thinning and metamorphism (Western Meseta, Morocco). *Pangea* **2000**, *33/34*, 27–47.
94. Simonet, C.; Fritsch, E.; Lasnier, B. A classification of gem corundum deposits aimed towards gem exploration. *Ore Geol. Rev.* **2008**, *34*, 127–133. [CrossRef]
95. Groat, L.A.; Laurs, B.M. Gem Formation, Production, and Exploration: Why Gem Deposits Are Rare and What is Being Done to Find Them. *Elements* **2009**, *5*, 153–158. [CrossRef]
96. Yakymchuk, C.; Szilas, K. Corundum formation by metasomatic reactions in Archean metapelite, SW Greenland: Exploration vectors for ruby deposits within high-grade greenstone belts. *Geosci. Front.* **2018**, *9*, 727–749. [CrossRef]
97. Lanari, P.; Wagner, T.; Vidal, O. A thermodynamic model for di-trioctahedral chlorite from experimental and natural data in the system MgO–FeO–Al_2O_3–SiO_2–H_2O: Applications to P–T sections and geothermometry. *Contrib. Mineral. Petrol.* **2014**, *167*, 968. [CrossRef]